2010-07-29

Using Design of Experiments and Electron Backscatter Diffraction to Model Extended Plasticity Mechanisms In Friction Stir Welded AISI 304L Stainless Steel

Benjamin D. Nelson
Brigham Young University - Provo

Using Design of Experiments and Electron Backscatter Diffraction to Model Extended Plasticity Mechanisms In Friction Stir Welded AISI 304L Stainless Steel

Benjamin D. Nelson

A thesis submitted to the faculty of
Brigham Young University
in partial fulfillment of the requirements for the degree of

Master of Science

Carl D. Sorensen, Chair
Tracy W. Nelson
Larry L. Howell

Department of Mechanical Engineering

Brigham Young University

December 2010

ABSTRACT

Using Design of Experiments and Electron Backscatter

Diffraction to Model Extended Plasticity Mechanisms

in Friction Stir Welded AISI 304L Stainless Steel

Benjamin D. Nelson

Department of Mechanical Engineering

Master of Science

Extended plasticity mechanisms (EPM) allow a metal to undergo extended plastic deformation without failure. These mechanisms are responsible for the extended plastic deformation characteristic of hot working processes. In this thesis it is shown that electron backscatter diffraction (EBSD) is capable of detecting EPM artifacts in the final microstructure of AISI 304L stainless steel (304L). Results also indicate that dislocation cells form in hot worked AISI 304L stainless steel.

Additionally, in this study EBSD data collection and analysis is used with a design of experiments approach to model the presence of EPM artifacts in the final microstructure of friction stir welded 304L. Texture analysis of the welded material reveals a dominant shear deformation texture and a lack of the rotated cube texture. The shear deformation texture is characteristic of dynamic recovery (DRV) and continuous dynamic recrystallization (CDRX), while the rotated cube texture is characteristic of discontinuous dynamic recrystallization (DDRX). The texture analysis results indicate that dynamic recovery (DRV) and continuous dynamic recrystallization (CDRX) play a role in the final microstructure of the welded material, while DDRX does not. Design of experiments was used to find the relationships between the fraction of cell boundaries and spindle speed, travel speed, location in the stir zone, and tool temperature. The regression analyses reported that predicted fraction of cell boundaries were relatively high (approximately 0.70 or more) and changed by less that 20% in the stir zone and 10% in the TMAZ. The relatively high predictions indicate that in FSW 304L DRV dominates and limited CDRX occurs. The small changes in predictions across the experimental space indicate that the effects, while statistically significant, are not practically significant. Finally, an alternate tool temperature basis was developed, which provides a valid method for selecting welds which should have constant tool temperature.

Keywords: Benjamin Nelson, FSW, 304L, EBSD, recovery, recrystallization, DRV, CDRX, DDRX, DOE

ACKNOWLEDGMENTS

I would like to thank Dr. Carl Sorensen and Dr. Tracy Nelson, whose mentorship has guided me in expanding and deepening my knowledge for this thesis. I would also like to thank my wife, Hannah, for her loyal support throughout my time at Brigham Young University. Finally, I would like to thank the Center for Friction Stir Processing, A National Science Foundation Industry/University Cooperative Research Center, whose funding made this research possible.

TABLE OF CONTENTS

LIST OF TABLES

LIST OF FIGURES

1 INTRODUCTION

Friction stir welding (FSW) is a joining process that was invented by The Welding Institute in 1991. A rotating non-consumable tool is used to generate frictional heating at the tool/work piece interface. The frictional heating is sufficient to soften the material, without melting, for stirring by the tool. The rotating tool stirs the softened material together resulting in solid state weld.

Deforming a metal at an elevated temperature allows it to undergo extended plastic deformation without the onset of failure. This type of extended plasticity behavior is characteristic of the hot deformation that accompanies friction stir welding (FSW). Studies of numerical simulations of FSW of metals have reported values of 1000%-5000% elongation in FSW AISI 304 stainless steel [1], 500%-900% elongation in FSW of aluminum alloys [2, 3, 4, 5], and 500% elongation in FSW of 1018 steel [6]. Extended plasticity mechanisms permit the metal to accommodate extended plastic deformation during the FSW process by rearranging stored strain energy into lower energy configurations. Dynamic recovery (DRV), continuous dynamic recrystallization (CDRX), and discontinuous dynamic recrystallization (DDRX) are the extended plasticity mechanisms referred to in this thesis.

FSW AISI 304L stainless steel (304L) is the focus of this thesis because sigma phase formation has been reported in the FSW of 304L by Park et al. [7]. Sigma phase is chromium rich phase which has a deleterious effect on the corrosion properties on

stainless steels. Past research has shown that the formation of sigma phase in austenitic stainless steels correlates extremely well with nucleation and recrystallization [8]. Consequently, DRV, CDRX, and DDRX are studied in this thesis because DDRX is a nucleation phenomenon, while DRV and CDRX are extended recovery phenomena. However, the formation of sigma phase in FSW 304L is not studied in this thesis. It is presented here only to give context for the motivation of this research.

Electron backscatter diffraction (EBSD) can be used to characterize the presence of extended plasticity mechanisms artifacts in a final microstructure. However, EBSD data is often only analyzed semi-quantitatively. This thesis presents a methodology and results for coupling EBSD data collection and analysis with a design of experiments approach to model the presence of extended plasticity mechanisms artifacts in the final microstructure of FSW 304L.

2 BACKGROUND

In this chapter the role and operation of extended plasticity mechanisms (EPM) are discussed. They are compared to static recovery (SRV) and static recrystallization (SRX) which gives EPM context for consideration. Following the discussion of EPM, a background of the FSW of 304L is presented. Finally, the capabilities of EBSD and quantitative analysis of EBSD data are discussed.

2.1 Extended Plasticity Mechanisms

The EPM studied in this thesis are dynamic recovery (DRV), continuous dynamic recrystallization (CDRX), and discontinuous dynamic recrystallization (DDRX). These EPM allow a metal to accommodate extended plastic deformation without the onset of failure. This is accomplished by rearranging stored strain energy (dislocations and vacancies) into lower energy configurations such as dislocation cell boundaries, or by annihilating stored strain energy through nucleation and recrystallization.

A brief summary of SRV and SRX are given here in order to give EPM a context for consideration. When a metal is cold worked a fraction of the energy that is used to plastically deform it is stored in the lattice as strain energy. SRV results in a modest reduction in stored strain energy by rearranging the dislocations. This is accomplished by elevating the temperature during a post-work heat-treatment sufficiently to facilitate the rearrangement of dislocations by diffusion. SRX results in a large reduction in stored

strain energy by replacing the deformed lattice with relatively strain-free lattice. This is accomplished by elevating the temperature during post-work heat-treatment sufficiently to facilitate the nucleation of new strain-free grains by diffusion. In the case of both SRV and SRX, the stored strain energy acts as a driving force for the phenomenon and temperature affects the kinetics of the phenomenon. For a given condition of stored strain energy, the temperature associated with SRX is always greater that the temperature associated with SRV.

EPM are similar to SRV and SRX, however, they are distinctly different, as well. Table 2-1, which is discussed below, compares EPM to SRV and SRX for FCC metals. The mechanism for SRV is dislocations moving into lower energy dislocation cell boundaries [9]. SRV of a deformed material results in a deformation texture [9, 10, 11]. The resulting morphology of SRV is deformed grains filled with subgrains (dislocation cells) [9].

The mechanism of DRV is the same as SRV, except that DRV occurs during hot deformation [9]. Like SRV, DRV results in a deformation texture and dislocation cell structure [9, 10, 11]. The resulting morphology of DRV is deformed grains filled with subgrains (dislocation cells) [9].

The mechanism of CDRX is similar to DRV, but it results in high angle boundaries without a nucleation event [9, 10]. Like DRV and SRV, CDRX results in a deformation texture [9, 10, 11]. The resulting dislocation structure of CDRX is subgrains that have evolved to low angle and high angle misorientation boundaries [9, 10]. The resulting morphology of CDRX is deformed grains filled with subgrains that have high angle boundaries [9, 10]. It is important to note that while CDRX is labeled as a

recrystallization phenomenon it is more accurately described as a recovery phenomenon because no nucleation event occurs [9, 10].

DDRX can take place in parallel with DRV. The mechanism of DDRX is nucleation of new strain-free grains during deformation [9]. DDRX results in a recrystallization texture which is distinctly different than a deformation texture [13]. The resulting dislocation structure of DDRX is a random structure that has higher dislocation density than SRX [9]. The resulting morphology of DDRX is refined equiaxed grains interspersed with deformed grains.

The mechanism of SRX is like that of DDRX, except that for SRX nucleation takes place during a post-work heat-treatment [9]. Like DDRX, SRX results in a recrystallization texture [12, 13, 14]. The resulting dislocation structure of SRX is a random structure that has relatively low dislocation density [9]. The resulting morphology of SRX is equiaxed grains [9].

Similar to the transition from SRV to SRX, DRV and CDRX transition to DDRX with increased driving force for nucleation. This increase in driving force can be accomplished by increasing the strain and/or strain rate. Increasing the temperature increases the kinetics of the phenomenon. The transition point from recovery phenomena to a nucleation and recrystallization phenomenon is dependent upon the stacking fault energy of the FCC metal. Stacking fault energy varies from high (aluminum) to medium (copper) to low (austenitic stainless steels, brass) [15, 16]. In general, high stacking fault energy metals tend to dynamically recover while low stacking fault energy metals tend to dynamically recrystallize [9, 17]. 304L dynamically recovers but possess sufficiently

low stacking fault energy to dynamically recrystallize when the critical strain for recrystallization for a given set of temperature and strain rate is exceeded [17].

Table 2- 1 Comparison of extended plasticity mechanisms (EPM) to static recovery (SRV) and static recrystallization (SRX) for FCC metals. The mechanism, resulting texture, resulting dislocation structure, and resulting morphology of each case are compared, which reveals that EPM have similarities with SRV and SRX but distinct differences, as well.

	Static Recovery (SRV)	**Dynamic Recovery (DRV)**	**Continuous Dynamic Recrystalliz-ation (CDRX)**	**Discontinuous Dynamic Recrystalliz-ation (DDRX)**	**Static Recrystalliz-ation (SRX)**
Mechanism	Dislocation movement to lower energy configurations (i.e. cell structure), no nucleation [9]	Same as SRV, but during hot deformation [9]	Similar to DRV, but results in high angle grain boundaries without nucleation [9,10]	Can take place in parallel with DRV. Nucleation occurs during deformation [9]	Nucleation takes place post deformation, during heat-treatment [9]
Resulting Texture	Deformation texture [9,10,11]	Deformation texture [9,10,11]	Deformation texture [9,10,11]	Recrystalliz-ation texture, distinctly different than deformation texture [13]	Recrystalliz-ation texture [12,13,14]
Resulting Dislocation Structure	Cell structure [9]	Cell structure [9]	Subgrains that evolve to low and high angle misorientation boundaries [9,10]	Higher dislocation density than SRX, random structure [9]	Relatively low dislocation density, random structure [9]
Resulting Morphology	Deformed grains filled with subgrains [9]	Deformed grains filled with subgrains [9]	Deformed grains filled with subgrains that have high angle boundaries [9,10]	Refined equiaxed grains	Equiaxed grains [9]

Stacking fault energy affects EPM of FCC metals because of its strong effect on dislocation mobility. In general, glide and climb are the two modes of dislocation

mobility. In the following paragraphs, stacking fault energy will be discussed, followed by discussions on how it affects dislocation glide and dislocation climb.

In FCC metals a dislocation can dissociate into two partial dislocations because it is energetically favorable. This produces a stacking fault between the partial dislocations. The stacking fault energy of the metal determines how far apart the partial dislocations can dissociate. High stacking fault energy metals have a higher energy per unit area of stacking fault than low stacking fault energy metals. Consequently, low stacking fault energy metals allow the partial dislocations to dissociate farther apart than high stacking fault energy metals. A pair of partial dislocations in this dissociated state is referred to as an extended dislocation [18].

Dislocation glide is primarily a function of stress. An extended dislocation is free to glide as long as there are no obstacles impeding its path of glide. Cross-slip or cross-glide is a special case of glide where an extended dislocation glides onto a new slip plane because of resistance to glide on its current slip plane. Dislocation climb is primarily a function of temperature (equilibrium vacancy concentration). Climb consists of diffusive motion of vacancies that can add to or take away from the extra half-planes of atoms which make up a dislocation. An extended dislocation must first constrict into a single dislocation in order to either cross-slip or climb. Consequently, a decrease in stacking fault energy of a metal makes the occurrence of cross-slip and climb more energetically costly [18, 19, 20].

Additionally, Kim et al. indicate climb and glide must occur together in order to form dislocation cell boundaries [21]. When considering the affects of stacking fault

energy on cross-slip and climb it becomes apparent that low stacking fault energy metals are less likely to form dislocation cells than high stacking fault energy metals.

2.2 Friction Stir Welding of AISI 304L Stainless Steel

FSW of 304L has not been studied extensively, as demonstrated by the small body of literature that exists on the subject. FSW of high melting temperature materials, such as 304L, requires more robust tools than those used for FSW of low melting temperature materials. Polycrystalline cubic boron nitride (PCBN) tools have been successfully used to FSW several high melting temperature materials, including 304L [22].

Studies have been carried out on the microstructure, mechanical properties, corrosion resistance, sigma phase formation, and residual stresses in FSW 304L [7, 23, 24]. Additionally, more in depth studies on the microstructure of FSW 304L have been carried out. Sato et al. used crystallographic texture analysis to locate regions of dynamic recrystallization and static recrystallization in the stir zone of FSW 304L [25]. However, Sato et al. did not use an appropriate sample coordinate system (which will be presented in this thesis) for texture analysis of FSW 304L. Park et al. identified regions of dynamically recovered and dynamically recrystallized regions in the stir zone of FSW 304L [26]. However, in that study Park et al. did not distinguish between CDRX and DDRX.

In summary, the appropriate sample coordinate system has not been used for crystallographic texture analysis of FSW 304L. Additionally, in terms of EPM, there has been no study which differentiates between DRV, CDRX, and DDRX in the final

microstructure of FSW 304L. Finally, there has been no study which has quantitatively analyzed crystallographic textures in FSW 304L, nor in which design of experiments has been used to empirically model EPM artifacts in the final microstructure of FSW 304L.

2.3 Electron Backscatter Diffraction Analysis of Microstructure and Texture

EBSD is fast approaching TEM capabilities in detecting certain microstructures. Compared to TEM, EBSD has much faster sample preparation times, and it proves easier for location specific sample examination. Richard et al. recently published a study where analyzed ESBD data was compared to TEM micrographs of the same area, which showed that EBSD is capable of detecting dislocation cells [27]. Humphreys published a review of the capabilities of EBSD for characterizing grain and subgrain microstructures. The review indicated that EBSD has at least 1° angular resolution, which is well suited for detection of dislocation cell boundaries [28].

EBSD data is often only semi-quantitatively analyzed, however, it inherently lends itself to quantitative analysis. Analyzed EBSD data can be used to produce microstructure images comparable to optical micrographs, but contain much more information because of the crystallographic orientation data stored for each pixel. The misorientation angles of the boundaries can be characterized, and the lengths of the corresponding boundaries can be determined.

EBSD data can also be used for the quantitative analysis of crystallographic textures. It has been shown that torsional simple shear deformation can result in the A, B, and C texture components [29, 30, 31, 32]. Figure 2-1 shows 111 pole figures for torsional simple shear deformation texture components for FCC metals. The axis labeled

Z is both the direction of the torsion axis and the direction of the shear plane normal (SPN). The axis labeled θ is the shear direction (SD). The radial direction (XD) goes into the plane of the pole figure. A texture component represented by {*hkl*}<*uvw*> is a plane {*hkl*} whose normal is near but not necessarily exactly the same as the direction SPN, and a direction <*uvw*> (usually a closed pack direction) near the macroscopic shear direction (SD) [29]. In this thesis, the A and A* components are considered together as one A component.

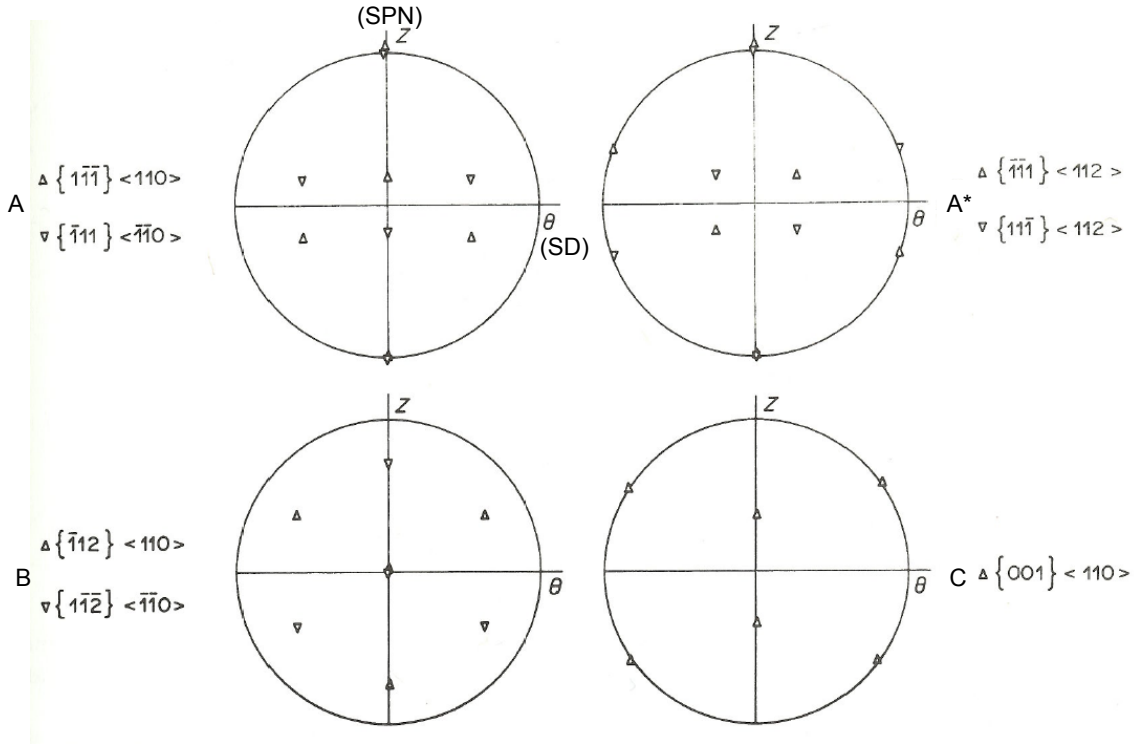

Figure 2- 1 111 pole figures showing torsional simple shear deformation texture components for FCC metals. The axis labeled Z is the direction of the torsion axis and the direction of the shear plane normal (SPN). The axis labeled θ is the shear direction (SD). The radial direction (XD) goes into the plane of the pole figure. A texture component represented by {hkl}<uvw> is a plane {hkl} whose normal is near, but necessarily exactly the same, as the direction of the SPN, and a direction <uvw> (usually a closed pack direction) near the macroscopic shear direction (SD) [29]. In this thesis, the A and A* components are considered together as one A component.

Bocher et al. found that hot torsion tested AISI 304 stainless steel produced a rotated cube texture that is characteristic of DDRX. More specifically, they reported that the rotated cube texture is characteristic of nucleation and grain growth in DDRX, which sets it apart from shear deformation textures [33]. The sample coordinate system of the rotated cube texture is the same as that of shear deformation texture components shown in Figure 2- 1.

Shear deformation textures are of significance in FSW materials because of shearing induced in the material around the pin. Fonda and Bingert [34] and Sato et al. [35] have shown that torsional simple shear deformation textures are found in FSW aluminum when the EBSD data is rotated to the shear deformation sample coordinate system.

3 EXPERIMENTAL METHOD

Three interrelated studies were carried out for this thesis. First, a cell structure investigation was carried out to verify dislocation cell formation in 304L and to verify EBSD capability to detect dislocation cells. Second, a gage capability study was carried out to determine smallest effect size that could be detected by the EBSD data collection and analysis process. Third, a study combining EBSD data collection and analysis with a DOE approach was carried out to study EPM artifacts in the final microstructure of FSW 304L. The experimental methods for all of these studies are presented in the following sections.

3.1 Cell Structure Investigation

The cell structure investigation was carried out to verify dislocation cell formation in 304L and to verify EBSD capability to detect dislocation cells. As stated in the background, low stacking fault energy metals are less likely to form dislocation cells than high stacking fault energy metals. It was suspected that the low stacking fault energy of 304L might inhibit dislocation cell formation in some cases. Consequently, cold working and hot working were used, because of large disparities in respective dislocation mobility, to examine the formation of dislocation cells in 304L. For cold working the material was cold rolled followed by a post-work heat-treatment. For hot working the

material was hot torsion tested. The details of the cell structure investigation are presented in the sections that follow.

3.1.1 Material

304L was used in this study. The cold rolling was carried out in 0.25 in. (6.35 mm) thick plate. Hot torsion testing samples were machined out of cylindrical bar stock.

3.1.2 Cold Rolling and Post-Work Heat-Treatment

Material was cold rolled with interpass quenching until 60% cold work was achieved. Dislocation climb mobility is limited in cold working, so the material was heat-treated to facilitate dislocation cell formation. The procedure to determine the appropriate post-work heat-treatment temperature was patterned after a method presented by Chowdhury et al. [36]. The cold rolled material was heat-treated at incrementally increasing discrete temperatures. Between each increase the material was quenched and tested for hardness until the recovery temperature was discovered. Once the recovery temperature was determined, cold rolled material was heat-treated at 700° C for 1 and 5 hours, 750° C for 1, 2, and 5 hours, and 650° C for 35 hours.

3.1.3 Hot Torsion Testing

Hot torsion testing was used because of the increased dislocation climb mobility during deformation due to elevated temperature. The specimen was machined according to the specifications published by Norton [37]. In order to produce a well recovered microstructure, and to avoid recrystallization, the specimen was tested at a relatively low strain and strain rate of 0.5 and 0.1 s^{-1}, at 1100° C.

3.1.4 Sample Preparation

Samples from the cold rolled material were excised using an abrasive water jet. As shown in Figure 3-1a, for the cold rolled specimen the rolling direction (RD) and transverse direction (TD) lie in the inspection plane. The normal direction is orthogonal to the inspection plane.

The gage length of the hot torsion test specimen was removed using a low speed diamond saw. Using the low speed diamond saw, the gage length was cut in half along the axis, as shown in Figure 3-1b, such that the axis lies in the inspection plane. The scan location is positioned at the outer radius, at the mid-plane of the gage length.

All specimens were mounted in Bakelite for grinding and polishing. The grinding consisted of 60, 120, 320, and 600 grit SiC abrasive paper. After grinding, the polishing consisted of 800 and 1200 grit SiC abrasive paper followed by 9, 6, 3, and 1 μm diamond pastes on Lecloth pads. Polishing was finished by vibrapolishing with colloidal silica on a Lecloth pad.

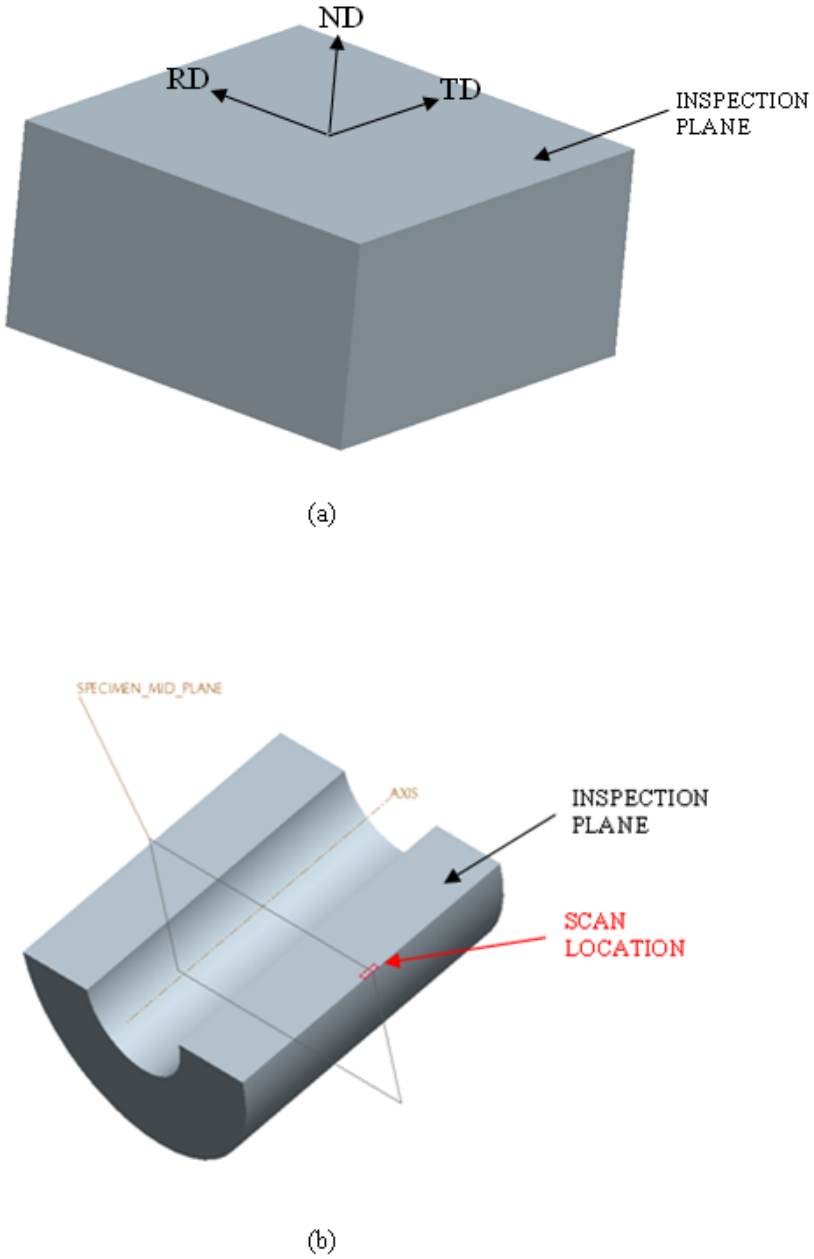

Figure 3- 1 Definitions of inspection planes relative to specimen geometries. (a) For the cold rolled specimen the rolling direction (RD) and transverse direction (TD) lie in the inspection plane. The normal direction (ND) is normal to the inspection plane. (b) Hot torsion specimen axis lies in the inspection plane. The scan location is located at the outer radius, at the mid-plane of the gage length.

3.1.5 Electron Backscatter Diffraction Data Collection and Analysis

EBSD data was collected on a Philips XL30 S-Feg using TSL OIM Data Collection 5 software. The samples were tilted 70° for scanning in the microscope. A 20 kV beam was used with a 12 mm working distance, spot size 5, and a 50 μm objective aperture. A 0.1 μm step size was used for the 700° C-1hour, 650° C-35 hours, and hot torsion specimens. A 0.5 μm step size was used for the remaining specimens. TSL OIM Data Analysis 5 software was used to generate image quality maps and grain boundary maps from the EBSD data.

3.2 Gage Capability Study

The gage capability study was carried out to determine the resolution capability of the EBSD data collection and analysis process. Typically a gage capability study is carried out on multiple parts that are nominally identical. Multiple measurements of the same feature on different nominally equivalent parts are made by multiple operators. This allows for a determination of the total measurement variation, and how the variation due to parts, variation due to the gage, and variation due to operators all contribute to the total measurement variation.

3.2.1 Material

Hot torsion tested 304L was used for the gage capability study. It was tested at a strain and strain rate of 0.5 and 0.1 s^{-1}, at 1100° C, which are the same parameters used in the cell structure investigation.

3.2.2 Sample Preparation

The gage length of the hot torsion tested specimen was cut with a low speed diamond saw, in the same manner as the hot torsion specimen in the cell structure investigation (see Figure 3-1b). The specimen was mounted in Bakelite for grinding and polishing. The grinding consisted of 60, 120, 320, and 600 grit SiC abrasive paper. After grinding, the polishing consisted of 800 and 1200 grit SiC abrasive paper followed by 9, 6, 3, and 1 μm diamond pastes on Lecloth pads. Polishing was finished by vibrapolishing with colloidal silica on a Lecloth pad.

3.2.3 Electron Backscatter Analysis Data Collection and Analysis

EBSD data was collected on a Phillips XL30 S-Feg using TSL OIM Data Collection 5 software. The samples were tilted 70° for scanning in the microscope. A 20 kV beam was used with a 12 mm working distance, spot size 5, 0.25 μm step size, and a 50 μm objective aperture. OIM Data Analysis 5 software was used to calculate fraction of cell boundaries (as explained in the next section in Equation 3-1).

Finding multiple nominally identical parts was problematic because the part feature to be measured was a microstructural characteristic (fraction of cell boundaries). Consequently, six distinct locations were used as six nominally identical parts, as shown in Figure 3-2. The locations were all situated at the outer radius of the specimen, within approximately ±0.059 in (1.5 mm) about the specimen mid plane along the specimen axis.

The microstructures (presence of cell boundaries and high angle boundaries) of the six different parts were considered nominally identical because they were all from

approximately the same location in the specimen and, consequently, had all experienced the same strain, strain rate, and temperature. Three measurements of the microstructure were taken from each part by one operator.

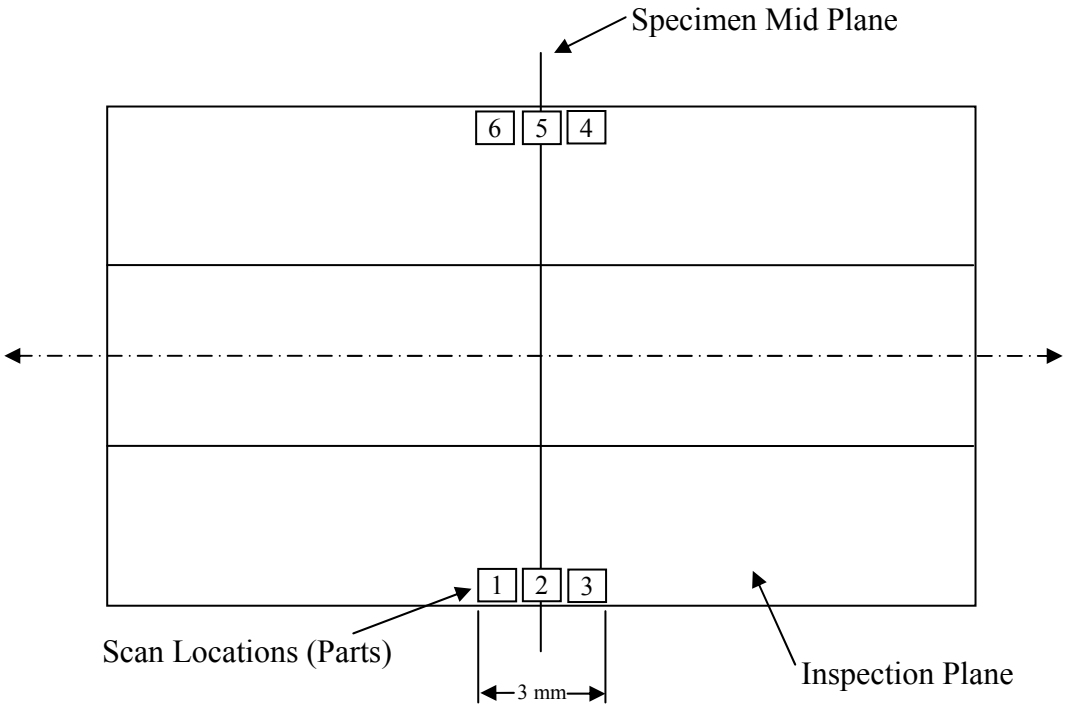

Figure 3- 2 Illustration of hot torsion tested 304L specimen used for the gage capability study. The specimen was sectioned and prepared identically to the specimen shown in Figure 3-1b. Six distinct locations were used as six nominally identical parts. The microstructures (dislocation cell boundaries) of the six different parts were considered nominally identical because they were from approximately the same location in the specimen and, consequently, had all experienced the same strain, strain rate, and temperature. Three measurements of the microstructure were taken from each part by one operator.

3.2.4 Statistical Analysis

As stated in the previous section, three measurements of the microstructural boundaries in each part were taken by one operator. The measurement of the lengths of cell boundaries (CB), low angle boundaries (LAB), and high angle boundaries (HAB) were used to determine the fraction of cell boundaries, as shown in Equation 3-1.

The variation due to operator becomes confounded with the variation due to the gage, because only one operator was used. Consequently, the variations due to operator and gage were lumped together as one source of variation due to the measurement process, and variation due to the part was considered as a second, separate source of variation. An analysis of variance (ANOVA) for two sources of variation was used to identify magnitudes of the variation due to the measurement process and the variation due to the part. Details of the analysis are shown in Appendix E.

3.3 Extended Plasticity Mechanisms in Friction Stir Welding Study

Once dislocation cell formation in 304L and EBSD capabilities were verified in the results of the cell structure investigation study, the EPM in FSW study was carried out using EBSD data collection and analysis and a DOE approach. The purpose of the EPM in FSW study was to model the presence of the EPM artifacts in the final microstructure of FSW 304L. FSW parameters were selected to fit a central composite design. EBSD data was collected and analyzed such that presence of EPM artifacts and crystallographic textures could be quantitatively analyzed. The fraction of different texture components was calculated and graphed. The presence of EPM artifacts was

modeled using linear regression to determine the effects and significance of the effects for the factors involved.

3.3.1 Material

304L was used in this study. The plates for friction stir welding were 0.25 in. (6.35 mm) thick and 6 in. (152.4 mm) wide.

3.3.2 Friction Stir Welding

Plates were ground prior to welding to remove oxide layer. Welds were performed in a bead-on-plate configuration along the center line of the width of the plates. Welds were performed with a PCBN tool (# E44036). The tool geometry was convex scrolled shoulder step spiral (CS4), as shown in Figure 3-3 on the next page.

The weld parameters were selected to fit a central composite design as shown in Figure 3-4 on the next page. The length of weld for each parameter was sufficient to allow the process to reach steady state. All of the welds were run at a constant machine depth of 0.166 in. The reported depth value was then adjusted to a more accurate depth value using a model for machine compliance. The details of the machine compliance model and the adjusted depth values are shown in Appendix A.

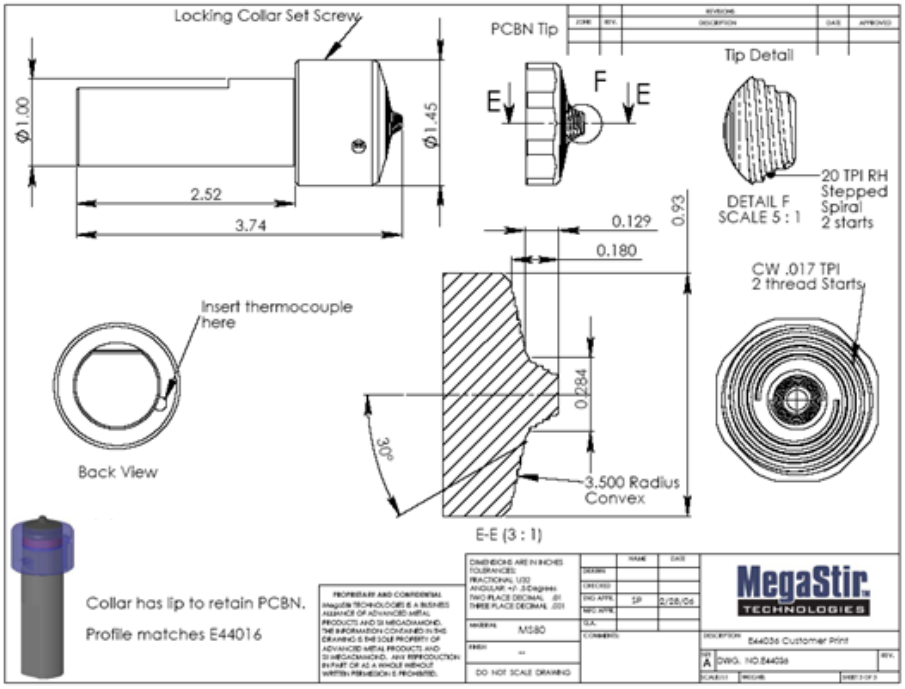

Figure 3- 3 Engineering drawing of the PCBN tool used to FSW 304L.

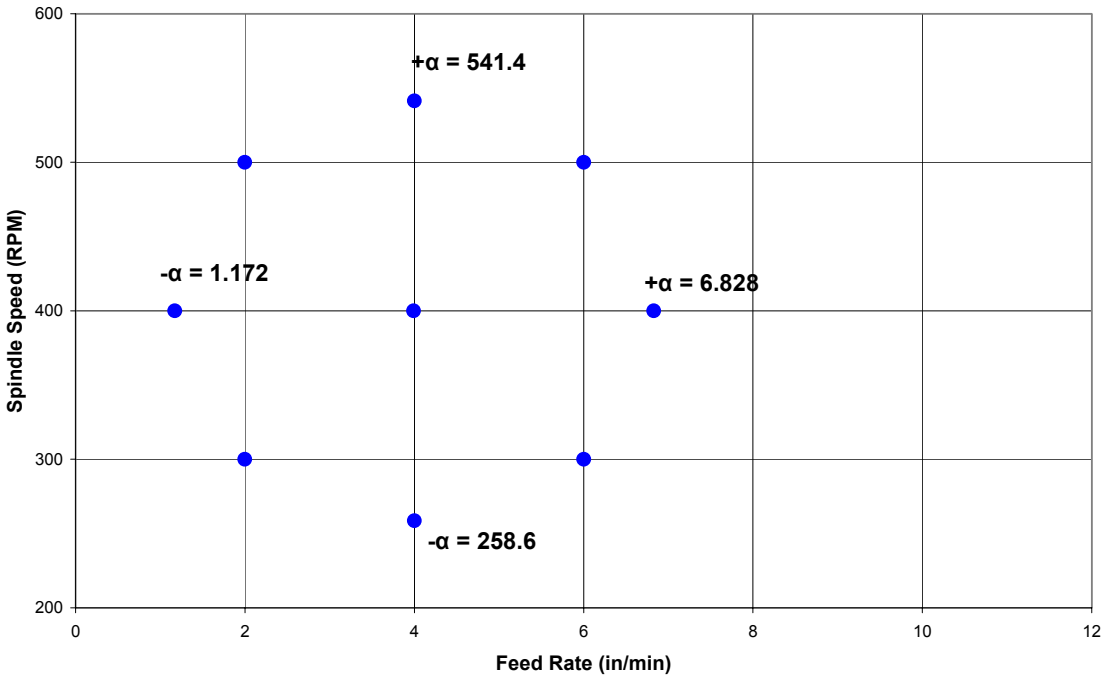

Figure 3- 4 Central composite design for FSW 304L.

3.3.3 Sample Preparation

Samples were excised from the welds using an abrasive water jet. Approximately 0.080 in. (2 mm) was ground from the surface of each sample for plan view examination. Only the pin affected region of the welds was examined in this study.

All specimens were mounted in Bakelite for grinding and polishing. The grinding consisted of 60, 120, 320, and 600 grit SiC abrasive paper. After grinding the polishing consisted of 800 and 1200 grit SiC abrasive paper followed by 9, 6, 3, and 1 μm diamond pastes on Lecloth pads. Polishing was finished by vibrapolishing with colloidal silica on a Lecloth pad. The final inspection plane depths, relative to the surface of the samples, after polishing are listed below in Table 3-1. The differences in inspection plane depth from sample to sample arose from grinding and polishing of the individual samples. More material was removed from some samples than others during the grinding and polishing process.

Table 3- 1 Final inspection plane depths after sample polishing, relative to the surface of the weld.

	400 rpm 1.17 ipm	**300 rpm 2 ipm**	**500 rpm 2 ipm**	**259 rpm 4 ipm**	**400 rpm 4 ipm**	**541 rpm 4 ipm**	**300 rpm 6 ipm**	**500 rpm 6 ipm**	**400 rpm 6.83 ipm**
Inspection Plane Depth	0.095 in.	0.087 in.	0.082 in.	0.088 in.	0.096 in.	0.087 in.	0.090 in.	0.095 in.	0.093 in.

The advancing side boundary, weld center, and retreating side boundary on each sample were marked with macrohardness indents. These indents served as fiducial marks to locate sample features in the microscope.

3.3.4 Electron Backscatter Diffraction Data Collection

EBSD data was collected on a Philips XL30 S-Feg using TSL OIM Data Collection 5 software. The samples were tilted 70° for scanning in the microscope. A 20 kV beam was used with a 12 mm working distance, spot size 5, and a 50 μm objective aperture. For each sample, locations at the thermomechanically affected zone (TMAZ), advancing side, weld center, and retreating side were scanned, as shown in Figure 3-5. Two additional replicates at the center point of the central composite design (see Figure 3) were collected.

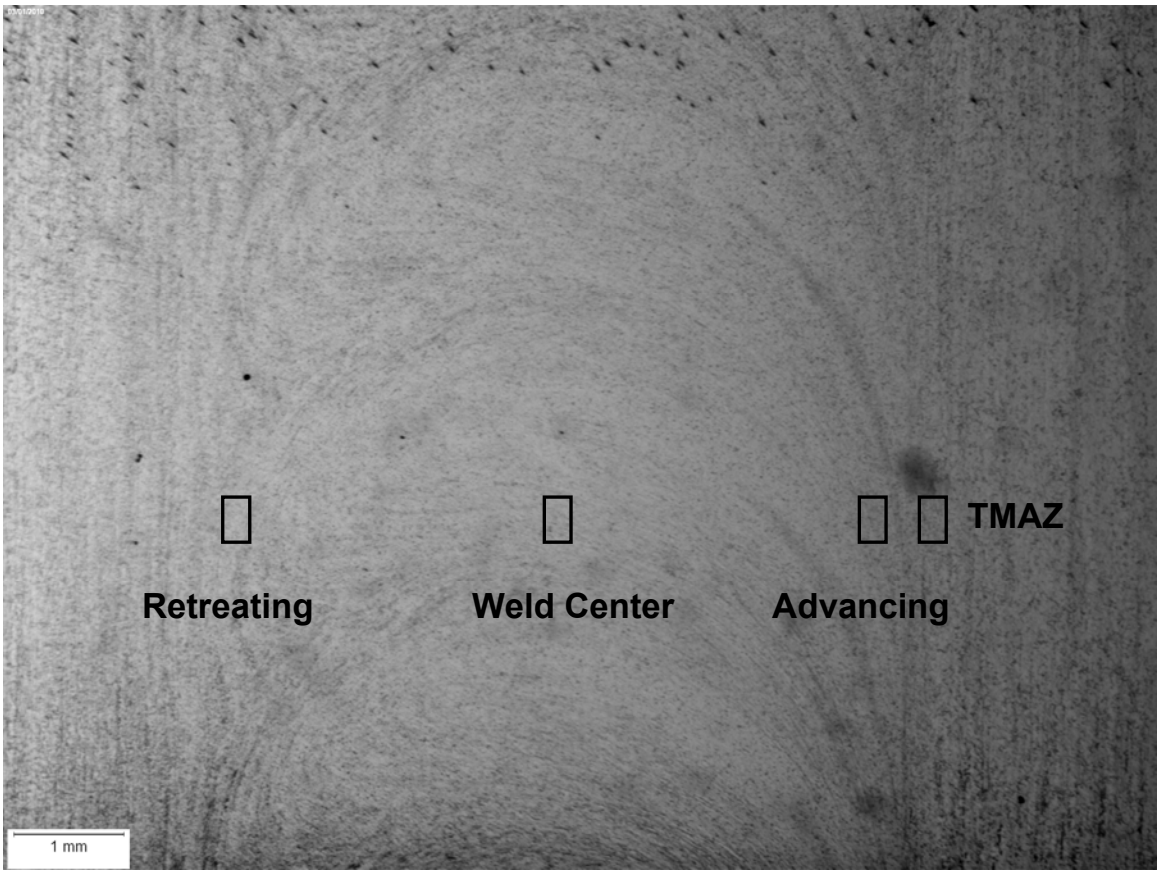

Figure 3- 5 Locations scanned on the surfaces of the FSW plan view samples.

For microstructure analysis a 30 μm x 90 μm area was scanned using a 0.25 μm step size. For texture analysis a 200 μm x 600 μm area was scanned using a 2 μm step size.

3.3.5 Electron Backscatter Diffraction Data Analysis

TSL OIM Data Analysis 5 software was used to analyze the EBSD data. Microstructure scan data analysis was carried out in the following manner. The minimum boundary threshold in the preferences of the software was set at 0.7°. The "Neighbor Orientation Correlation" clean up routine was used clean up the data sets. In that clean up routine the grain tolerance angle was set at 0.3°, the minimum confidence index was set at 0.5, and the clean level was set as 4. Grain boundary maps were generated and the total boundary lengths were determined for 0.7° - 5.0° misorientation boundaries , 5.0° - 15.0° misorientation boundaries , and 15.0° - 180.0° misorientation boundaries. The 0.7° - 5.0° misorientation boundaries are indicative of dislocation cell boundaries (CB), the 5.0° - 15.0° misorientations boundaries are indicative of low angle boundaries (LAB), and the 15.0° - 180.0° misorientation boundaries are indicative of high angle boundaries (HAB). The data for these different types of boundaries was used to formulate a ratio, shown below in Equation 3-1, which represents the fraction of dislocation cell boundaries.

$$\text{Fraction of Cell Boundaries} = \frac{\text{CB}(\text{mm})}{(\text{CB}(\text{mm}) + \text{LAB}(\text{mm}) + \text{HAB}(\text{mm}))} \qquad (3\text{-}1)$$

The presence of twins was found to have a biasing effect on HAB in the TMAZ data. To mitigate this effect, the lengths of Σ3 and Σ9 twin boundaries were determined and subtracted from the overall length of HAB in TMAZ data sets.

Figure 3-6 shows the sample coordinate system for simple shear deformation at the weld center behind the pin. Figure 3-6a illustrates {111} tetrahedrons formed at the weld center during welding. The <111> direction tilts 30° directly downward from the welding direction to accommodate the 30° angle of the truncated cone pin. The step spiral feature (threads) on the pin causes downward flow along the pin surface, resulting in the approximate 40° tilt of the <110> direction (shear direction). The RD-TD-ND coordinate system is assigned by the EBSD data collection software, while the SPN-SD-XD (shear plane normal - shear direction - radial direction) sample coordinate system [29, 30, 31, 32] is that of shear deformation at the weld center behind the pin. Figure 3-6b illustrates {111} planes at the weld center aligning with the 30° angle of the truncated cone pin. Figure 3-6c illustrates the SPN-SD-XD sample coordinate system from directly behind the tool at the weld center. The sample coordinate system is viewed directly down the <111> direction (the direction of the shear plane normal). The step spiral feature (threads) on the pin causes downward flow along the pin surface, resulting in the approximate 40° tilt of the shear direction.

Texture analysis is meaningful only if the sample coordinate system of deformation process is oriented to match the sample coordinate system of the texture in question. The EBSD data was rotated about the rolling direction (RD), transverse direction (TD), and normal direction (ND) in order to orient SPN-SD-XD sample coordinate system to that shown in the 111 pole figures in Figure 2-1. The nominal

rotation values (RD, TD, ND) for each location in the stir zone are as follows: retreating side (40°, -150°, 90°), weld center (40°, -150°, 0°), advancing side (40°, -150°, -90°), and TMAZ (40°, -150°, 90°). The actual rotation values for each location scanned in each weld are shown in Appendix B.

Adjustments of the nominal rotations were made in order to make the texture components in 111 pole figures match, as closely as possible, the locations of the ideal simple shear texture components shown in Figure 2-1. Similar rotations of EBSD data from FSW materials have been made by Fonda and Bingert [34] and Sato et al. [31].

Quantitative analysis of the texture components were carried out using TSL OIM Data Analysis 5 software. As stated in the background chapter, the ideal shear deformation texture consists of A, B, and C components. The OIM Analysis software was used to determine what fraction of pixels matched (within a 15° tolerance) the ideal shear deformation texture components. Additionally, the OIM Analysis software was used to determine what fraction of pixels matched (within a 15° tolerance) the rotated cube texture (DDRX texture) reported by Bocher et al. [33].

Special notice should be taken when entering the texture components into the OIM Analysis software because it is based on a rolling deformation sample coordinate system. Consequently, the texture components were rotated 90° about TD and 90° about ND in order to put them into the appropriate sample coordinate system for rolling deformation sample coordinate system software. A simple *.ang* file can be created wherein the Euler angles of the texture components are entered. The file can be opened in OIM Analysis and rotated. Additionally, pole figures and orientation distribution functions can be made to ensure that the texture components are appearing in the

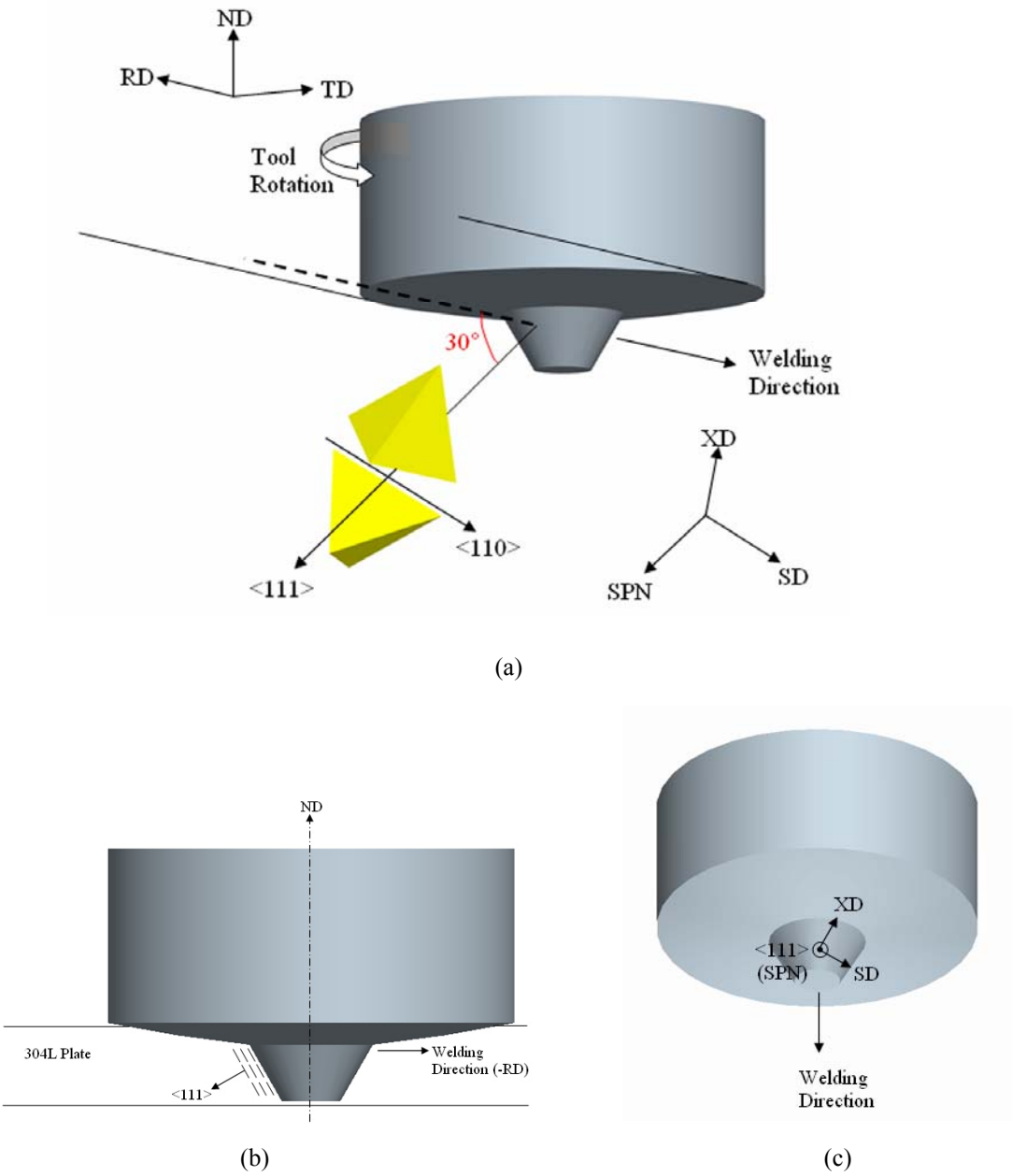

Figure 3- 6 Illustration of simple shear deformation of material at the weld center behind the pin, and corresponding sample coordinate system. (a) Illustration of {111} tetrahedrons formed at the weld center during welding. The <111> direction tilts 30° from the welding direction to accommodate the 30° angle of the truncated cone pin. The step spiral feature (threads) on the pin causes downward flow along the pin surface, resulting in the approximate 40° tilt of the <110> direction (shear direction). The RD-TD-ND (rolling direction-transverse direction-normal direction) coordinate system is assigned by the EBSD data collection software, while the SPN-SD-XD (shear plane normal-shear direction-radial direction) sample coordinate system is that of shear deformation at the weld center. (b) Illustration of {111} planes at the weld center aligning with the 30° angle of the truncated cone pin. (c) Illustration of SPN-SD-XD sample coordinate system viewed directly behind the tool at the weld center. The sample coordinate system is viewed down the <111> direction (the direction of the shear plane normal). The step spiral feature on the pin causes downward flow along the pin surface, resulting in the approximate 40° tilt of the shear direction.

appropriate locations. The rotated Euler angle values for rotated cube texture and the A, B, and C components of the shear deformation texture are shown in Appendix B.

3.3.6 Regression Analyses

Three distinct regression analyses were performed in this study. The first regression analysis found the relationship between fraction of cell boundaries and spindle speed, travel speed, and location in the stir zone. In the analysis spindle speed, travel speed, and location in the stir zone are represented by, respectively, X1, X2, and X3. See Appendix C for the layout of the factor matrix.

Tool temperature data was collected during the welds, but it was correlated with spindle speed and travel speed. This created the need for a dimensionally equivalent alternate basis in which the effect of tool temperature on the fraction of cell boundaries could be evaluated.

A second, intermediate, regression analysis was used to find the relationship between tool temperature and spindle speed and travel speed. Using the relationship from the regression analysis, Equation 3-2 was derived, by transforming the tool temperature data, such that θ, an adjusted tool temperature, passes through the origin of spindle speed-travel speed (X1-X2) basis. The details of the regression analysis and the formation of the alternate basis can be found in Appendix D.

$$\theta = T_{tool} - A_o \tag{3-2}$$

where A_o is the regression analysis intercept value.

The Gram-Schmidt Process [38] was used to find a vector, α, that is orthogonal to the vector θ, forming a θ-α alternate basis. This alternate basis was orthonormalized to

form an orthonormal θ-α-X3 alternate basis which is dimensionally equivalent to the X1-X2-X3 basis. The alternate basis was used in a third regression analysis to find the relationship between fraction of cell boundaries and θ, α, and X3. This allowed for direct comparison of the θ, α, and X3 regression analysis results with X1, X2, and X3 regression analysis results.

Regression models obtained from the two distinct bases were compared to ensure that the regression using the alternate θ-α-X3 basis produced a valid model. If linear models were obtained using both bases, a simple comparison of the of the model coefficients was conducted. If the models were of different orders from one basis to the next, then a process of substitution was used for direct comparison of the models.

In all cases, one at a time backward elimination was used to remove insignificant terms from the model. Any insignificant factors that might remain in the models are present in order to satisfy the requirements of a well-formulated model [39, 40].

4 RESULTS AND DISCUSSION

In this section the results of the cell structure investigation, gage capability study, and the EPM in FSW study are presented. For each study, the discussion and the results are presented in the same section.

4.1 Cell Structure Investigation

The cell structure investigation was carried out to verify both the formation of dislocation cells and the capabilities of EBSD in detecting cells in 304L. The results of the cold rolled/heat-treated materials are presented first, followed by the hot torsion tested material.

4.1.1 Cold Rolled and Post-Work Heat-Treated Materials

Only image quality maps were generated for the cold rolled/heat-treated material, because the deformation in the material made the grain boundary maps difficult to interpret. In the image quality maps white or light gray represent relatively high image quality, while black represents the lowest image quality where the data collection software can not identify the orientation. Typically, deformation free material (recrystallized grains) has a very high image quality, while highly deformed material has a relatively low image quality because the software can not readily identify the orientation of the material. Grain boundaries also have low image quality because there

is no single unique orientation. This is because the interaction volume of the beam encompasses material from both adjacent grains making it difficult for the software to identify the orientation of the boundary.

Image quality maps for 304L that was cold rolled and heat treat at 700° C for 1 and 5 hours are shown in Figures 4-1a and 4-1b. The image quality map for the material heat treated for 1 hour is shown in Figure 4-1a. The image quality map shows many high image quality, small recrystallized grains and nuclei clumped together in low image quality, deformed grains. Figure 4-1b shows the image quality map for the material heat-treated for 5 hours. The image quality map, like that of the 1 hour material, exhibits many high image quality, small recrystallized grains and nuclei clumped together in low image quality, deformed grains. In both cases no evidence of well defined dislocation cells can be seen.

The image quality maps for 304L cold rolled and heat-treated at 750° C for 1, 2, and 5 hours are shown in Figure 4-2. Figure 4-2a shows a majority of high image quality recrystallized grains and nuclei in the material heat-treated for 1 hour. Figure 4-2b shows an increase in high image quality recrystallized grains in the material heat-treated for 2 hours. Figure 4-2c shows complete recrystallization and consumption of low image quality, deformed grains in the material heat-treated for 5 hours. In all three cases no evidence of well defined dislocation cells can be seen.

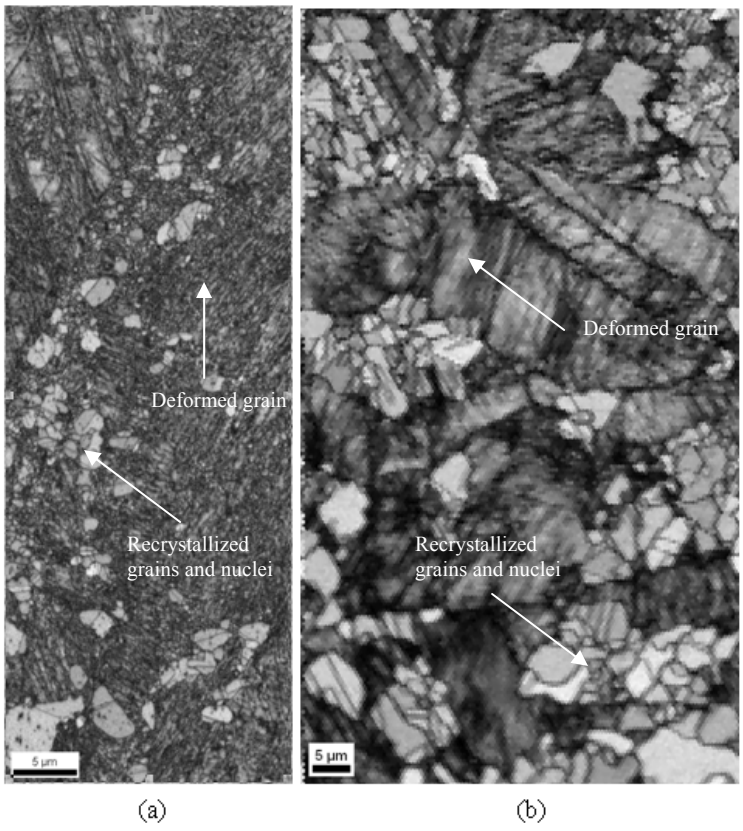

Figure 4- 1 Image quality maps for cold rolled 304L heat-treated at 700° C. (a) Material heat-treated for 1 hour, showing many high image quality, small recrystallized grains and nuclei clumped together in low image quality, deformed grains. (b) Material heat-treated for 5 hours, showing many high image quality, small recrystallized grains and nuclei clumped together in low image quality, deformed grains. In both cases, no clear evidence of dislocation cells can be seen.

The image quality map for 304L cold rolled and heat-treated at 650° C for 35 hours is shown in Figure 4-3. High image quality, small recrystallized grains can be seen clumped inside the low image quality, deformed grains. No evidence of well defined dislocation cells can be seen in the map.

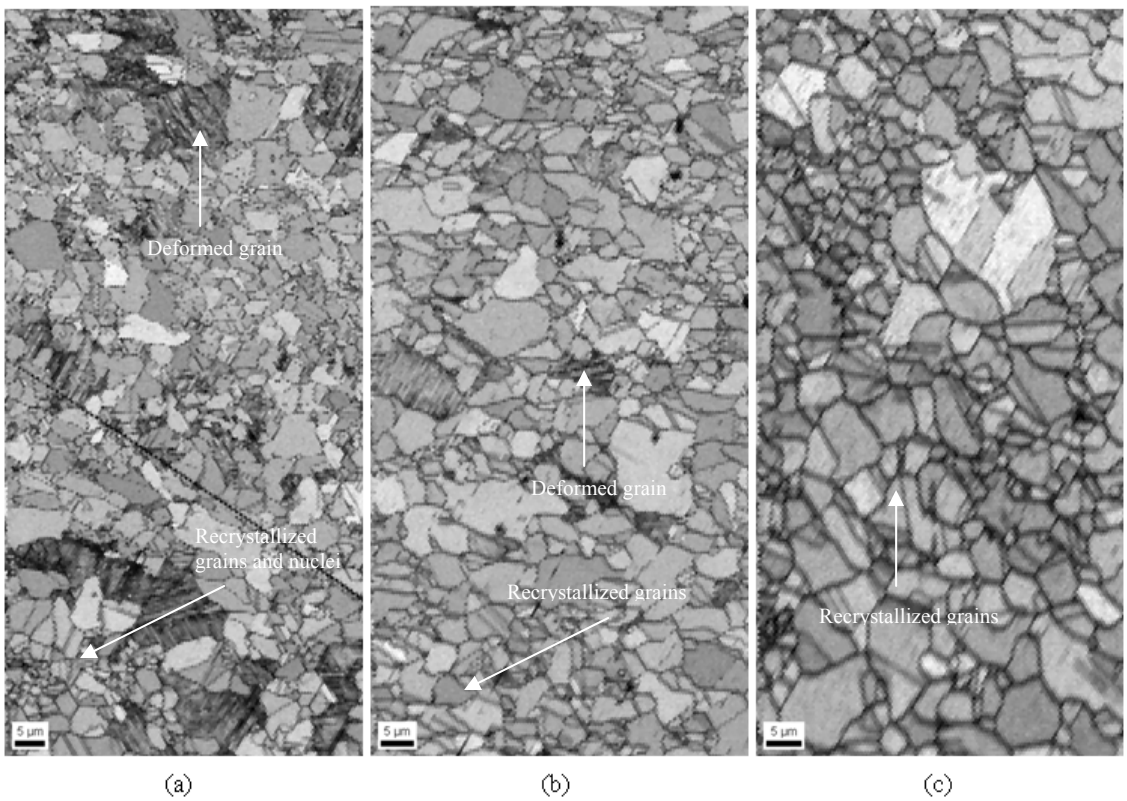

Figure 4- 2 Image quality maps for cold rolled 304L heat-treated at 750° C. (a) Material heat-treated for 1 hour, showing a majority of high image quality recrystallized grains and nuclei. (b) Material heat-treated for 2 hours, showing an increase in high image quality recrystallized grains. (c) Material heat-treated for 5 hours, showing complete recrystallization and consumption of low image quality, deformed grains.

The lack of well defined dislocation cells in the material that was cold rolled and heat-treated indicates that the mechanisms of static recovery is insufficient to form dislocation cells in 60% cold rolled 304L. A possible explanation for the lack of well defined dislocation cells is that the cold rolling was dominated by dislocation glide, but lacked the elevated temperature required for dislocation climb. Post-work heat-treatment was dominated by dislocation climb, but lacked the stress required for prolonged dislocation glide.

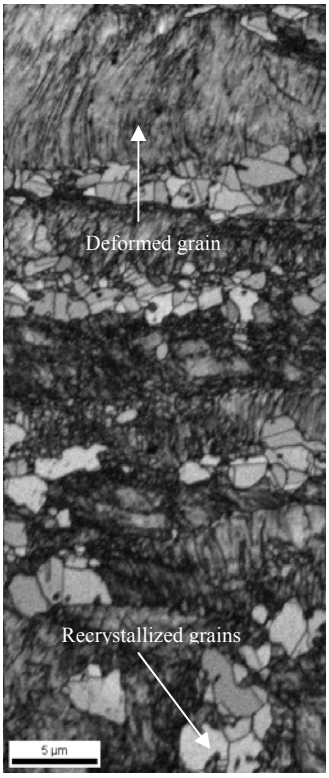

Figure 4- 3 Image quality map for cold rolled 304L heat-treated at 650° C for 35 hours. The map shows high image quality, small recrystallized grains clumped inside the low image quality, deformed grains.

4.1.2 Hot Torsion Tested Material

The image quality map and grain boundary map of the hot torsion tested 304L is shown in Figures 4-4a and 4-4b. Figure 4-4a shows the image quality map which exhibits both grain boundaries, which are dark black, and dislocation cell boundaries, which are lighter gray. The grain boundary map in Figure 4-4b confirms the interpretation of Figure 4-4a by identifying and distinguishing dislocation cell boundaries and high angle grain boundaries. As the key to the grain boundary map indicates, the dislocation cell boundaries (0.7-5.0° boundaries) are highlighted red, the low angle boundaries (5.0-15.0° boundaries) are highlighted green, and the high angle boundaries (15.0-180.0° boundaries) are highlighted blue.

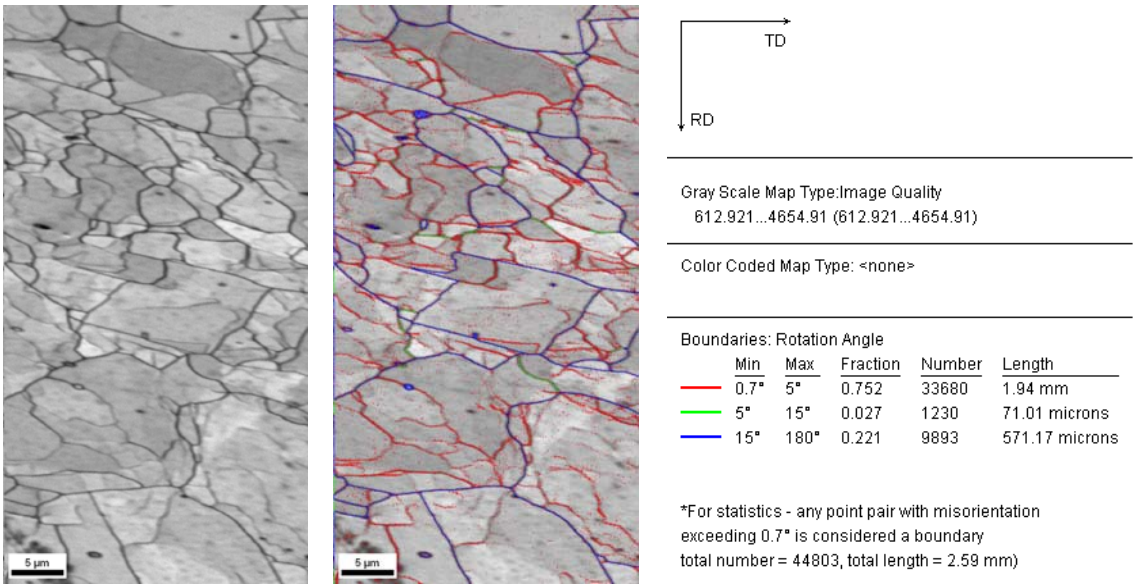

(a) (b)

Figure 4- 4 Image quality map and grain boundary map for hot torsion tested 304L. (a) Image quality map for hot torsion tested material, showing grain boundaries, which are dark black, and dislocation cell boundaries, which are lighter gray. (b) Grain boundary map for same material as (a), which identifies different misorientation boundaries. The colors in the map show a clear distinction between grain boundaries (blue) and dislocation cell boundaries (red).

The presence of well defined dislocation cells in the hot torsion tested material adds credence to the explanation for the lack of well defined dislocation cell in the material that was cold rolled and heat-treated. The dislocation cells in the hot torsion tested material are evidence of DRV and possibly CDRX. The conditions of the hot torsion testing allowed for dislocation glide, which requires stress, and dislocation climb, which requires elevated temperature. Additionally, the presence of dislocation cells in the material verifies that dislocation cells form in hot worked 304L and that EBSD can detect dislocation cells in 304L.

4.2 Gage Capability Study

Three fraction of cell boundaries measurements (see Equation 3-1) were made on each of the six parts by one operator using the EBSD data collection and analysis process. The analysis of variance (ANOVA) performed on the fraction of cell boundaries measurements determined that when using the EBSD data collection and analysis process, 0.021 was the magnitude of the smallest detectable effect on the fraction of cell boundaries (see Appendix E for details of the analysis). Suppose a regression analysis on the fraction of cell boundaries indicates that an effect, whose magnitude is smaller than 0.021, is significant. The gage capability study indicates that one can not be sure whether such an effect was actually caused by a change in factor settings or is simply noise in the data due to variability in both the gage and the operator. When one interprets regression analyses, it is important to note that the effect is equal to twice the coefficient reported by the analysis (effect = 2*coefficient).

4.3 Extended Plasticity Mechanisms in Friction Stir Welding Study

The results of the EPM in FSW study are presented in this section. The results will be presented in the order of texture analysis and microstructure analysis, followed by regression analyses for the fraction of cell boundaries in the stir zone and TMAZ.

4.3.1 Texture Analysis

The EBSD data files were rotated to the shear deformation sample coordinate system using 111 pole figures to ensure that the appropriate rotation had been performed. This was accomplished by comparing the texture components in the EBSD data pole

figures to the locations of the ideal A, B, and C shear deformation texture components shown in Figure 2-1. Figure 4-5 shows 111 pole figures created from rotated EBSD scans of locations in a weld. The difference in the pole figures is an example of texture components changing in any given weld. Figure 4-5a shows a well defined B component with the highest intensities at the locations of an ideal B component, which are marked with triangles (see Figure 2-1). Figure 4-5b shows less defined shear deformation texture components accompanied by random texture.

The OIM Analysis software was used to generate a crystal orientation map which identifies what fraction of pixels in the EBSD data correspond to a prescribed texture component (within a 15° tolerance). Figure 4-6 is an example of a crystal orientation map that identifies grains that have a shear deformation texture. In this example, the map was analyzed for the B component of the shear deformation texture. The grains which are highlighted blue correspond to the B component. The OIM Analysis software was used to determine the fraction of pixels that correspond to the B component, within a 15° tolerance. Similar crystal orientation maps were generated for every scanned location in the weld samples in order to determine the fraction of pixels that corresponds to the rotated cube texture and the A, B, and C components of the shear deformation texture.

The texture component fractions were calculated and plotted. The plots show the data with respect to the run order (see factor matrix in Appendix C). Figure 4-7 shows a stacked bar plot of the texture components for the retreating side of stir zone. The figure shows that shear deformation texture, particularly the A and B components, makes up more than 90% of the plotted texture components. This is result is indicative of a deformed microstructure.

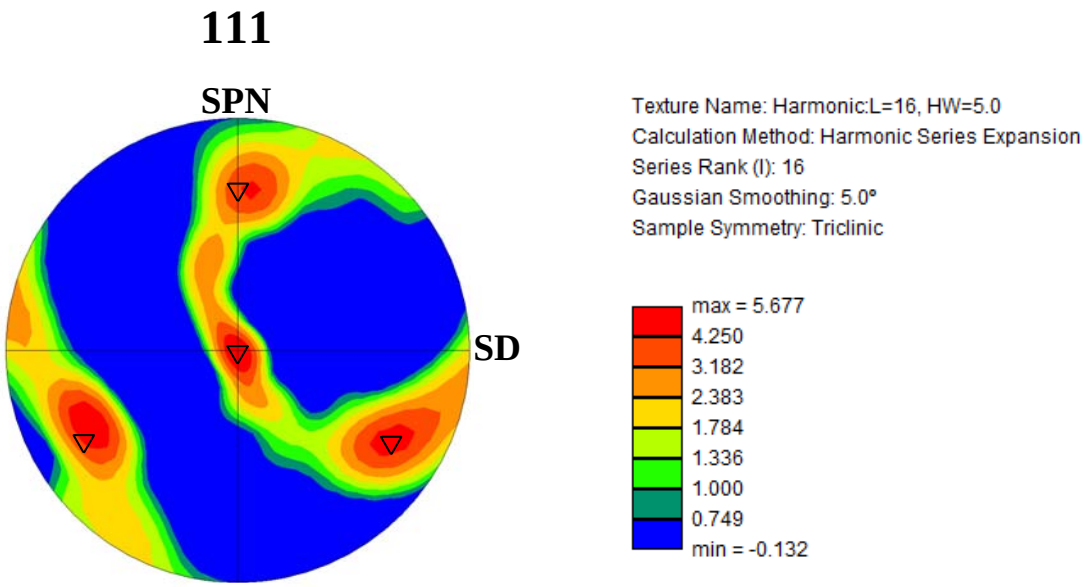

(a)

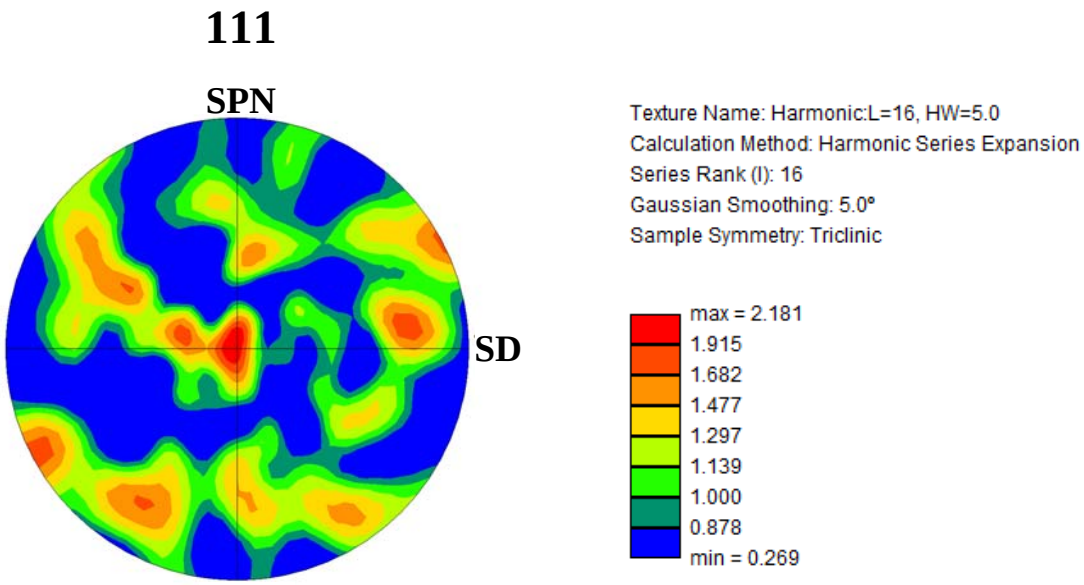

(b)

Figure 4- 5 111 pole figures created from rotated EBSD scans of locations in the weld. The difference in the pole figures is an example of texture components changing in the weld. (a) Example of a well defined B component with the highest intensities at the locations of an ideal B component, which are marked with the triangles (see Figure 2-1). (b) Example of a less defined shear deformation texture accompanied by random texture.

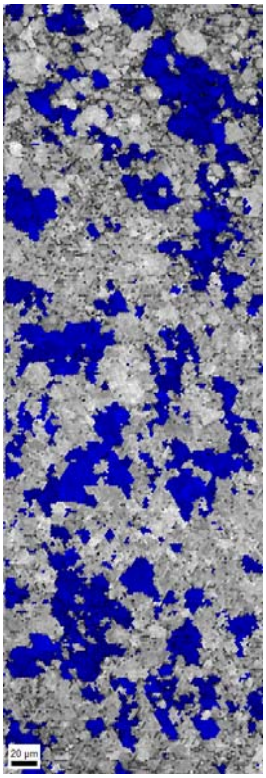

Figure 4- 6 Example crystal orientation map that identifies what grains have a shear deformation texture. In this example map was analyzed for the B component of the shear deformation texture. The grains which are highlighted blue correspond to the B component, within a 15° tolerance.

Figure 4-8 shows a stacked bar plot of the texture components in the center of the stir zone. Again, the shear deformation texture (largely the A and B components) makes up more than 90% of the plotted texture components. As before, this is indicative of a deformed microstructure.

Figure 4-9 shows a stacked bar plot of the texture components in the advancing side of the stir zone. As before, the shear deformation texture (largely the A and B components) makes up more than 90% of the plotted texture components. This is, again, indicative of a deformed microstructure.

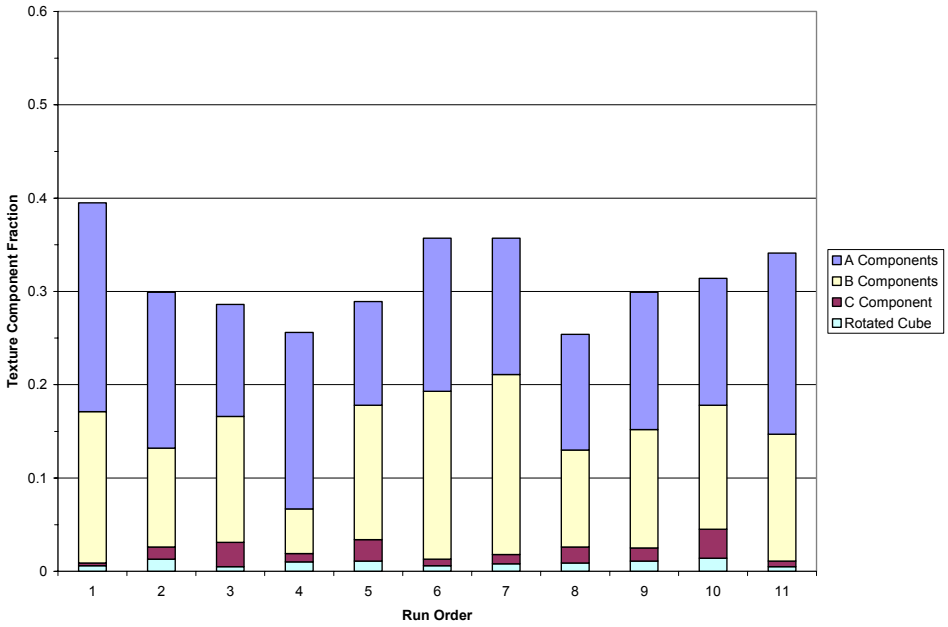

Figure 4- 7 Stacked bar plot of the different texture components at the retreating side of the stir zone. The run order is listed in the factor matrix of Appendix C. The shear deformation texture, particularly, the A and B components contribute more than 90% of the plotted texture components. This result is indicative of the deformed microstructure.

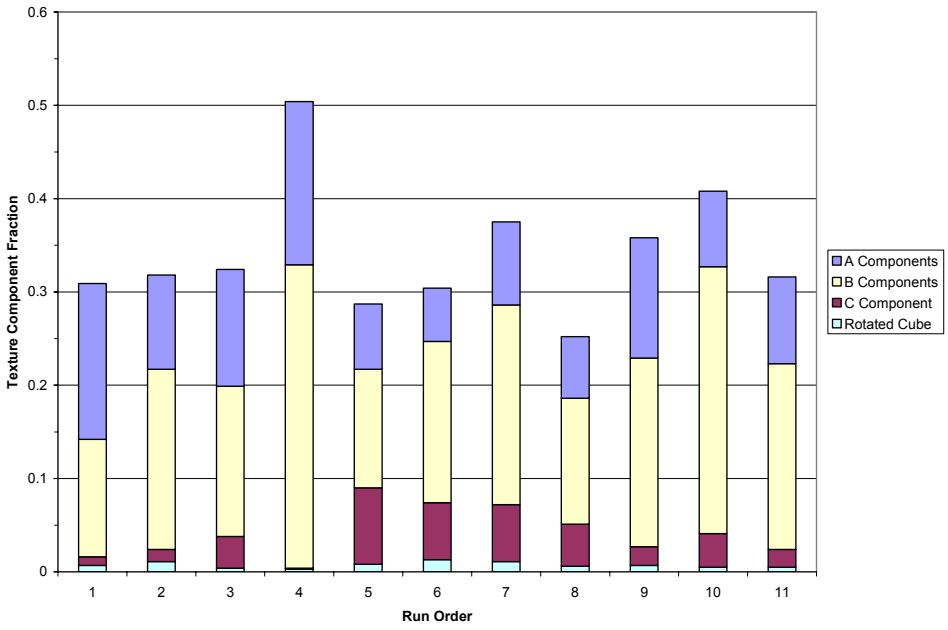

Figure 4- 8 Stacked bar plot of the different texture components at the center of the stir zone. The run order is listed in the factor matrix of Appendix C. The shear deformation texture (largely the A and B components) makes up more than 90% of the plotted texture components. This result is indicative of a deformed microstructure.

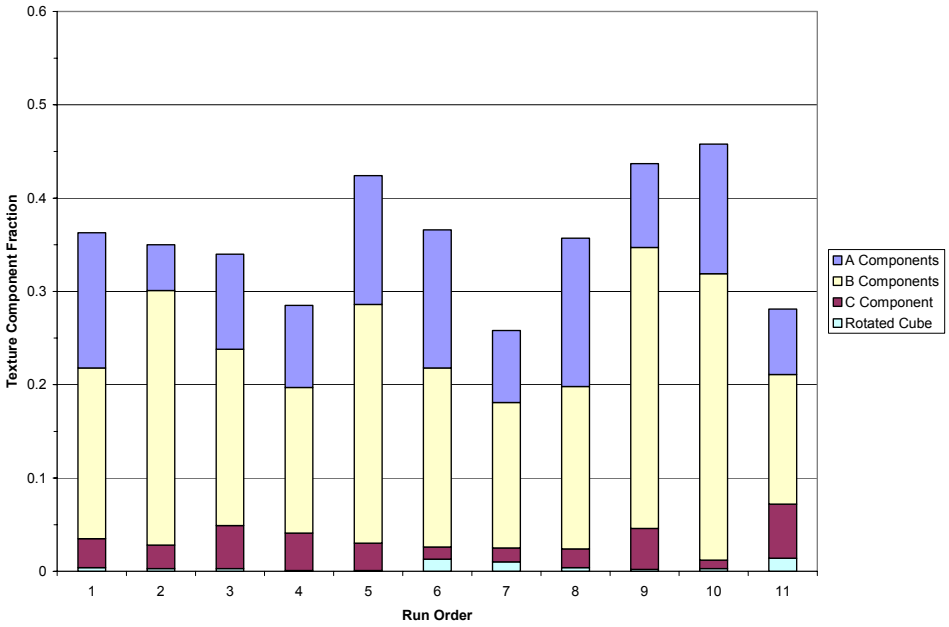

Figure 4- 9 Stacked bar plot of the different texture components at the advancing side of the stir zone. The run order is listed in the factor matrix of Appendix C. The shear deformation texture (largely the A and B components) makes up more than 90% of the plotted texture components. This result is indicative of a deformed microstructure.

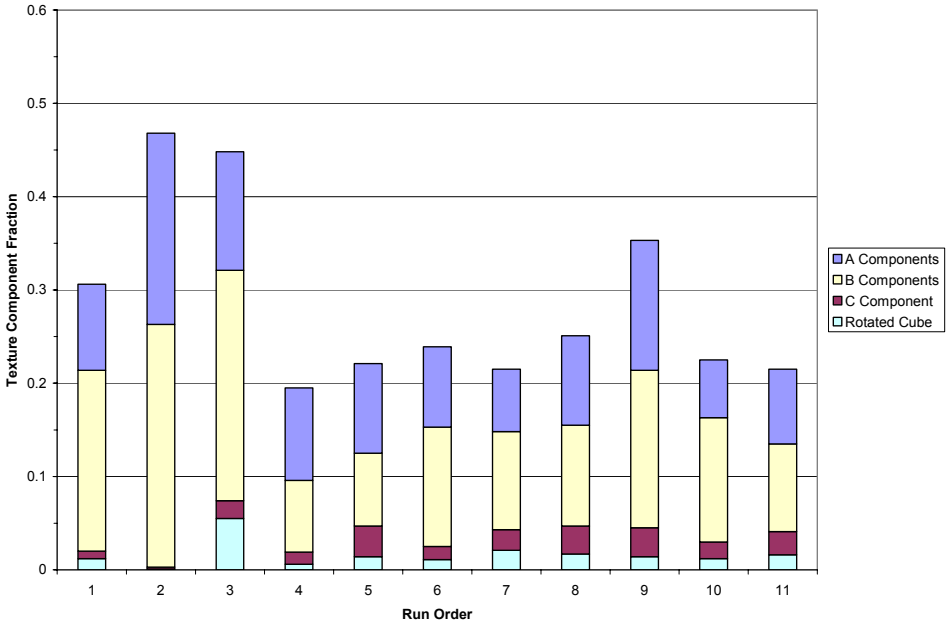

Figure 4- 10 Stacked bar plot of the different texture components at the TMAZ. The run order is listed in the factor matrix of Appendix C. The shear deformation texture (largely the A and B components) makes up more than 88% of the plotted texture components. This result is indicative of a deformed microstructure.

Figure 4-10 shows a stacked bar plot of the texture components at the TMAZ. The shear deformation texture (largely the A and B components) makes more than 88% of the plotted texture components. This result is indicative of a deformed microstructure.

The near absence of the rotated cube texture in the FSW 304L indicates that material that has undergone DDRX is not present in the final microstructure. Additionally, the dominant presence of the shear deformation texture components is indicative of DRV and CDRX, because they are recovery phenomena that retain the majority of the strain energy stored in the lattice. Consequently, only DRV and CDRX are considered as active EPM which produce EPM artifacts in the final microstructure of FSW 304L. The fraction of cell boundaries then has the following interpretation. An increase in the fraction of cell boundaries indicates DRV is becoming more dominant. A decrease in the fraction of cell boundaries indicates CDRX is becoming more dominant. This is because the end result of DRV is dislocation cells, an increase of which increases the fraction cell of cell boundaries. In contrast, the end result of CDRX is low angle and high angle boundaries, an increase of which decrease the fraction of cell boundaries.

4.3.2 Microstructure Analysis

A grain boundary map for the base metal of the FSW 304L plate is shown in Figure 4-11. The map shows large statically recrystallized grains that are relatively free of deformation. The fraction of cell boundaries (Equation 3-1) was not calculated for the base metal because the measure of cell boundaries does not make physical sense for statically recrystallized material. The grain boundary map is shown here for purposes of comparison to the FSW material.

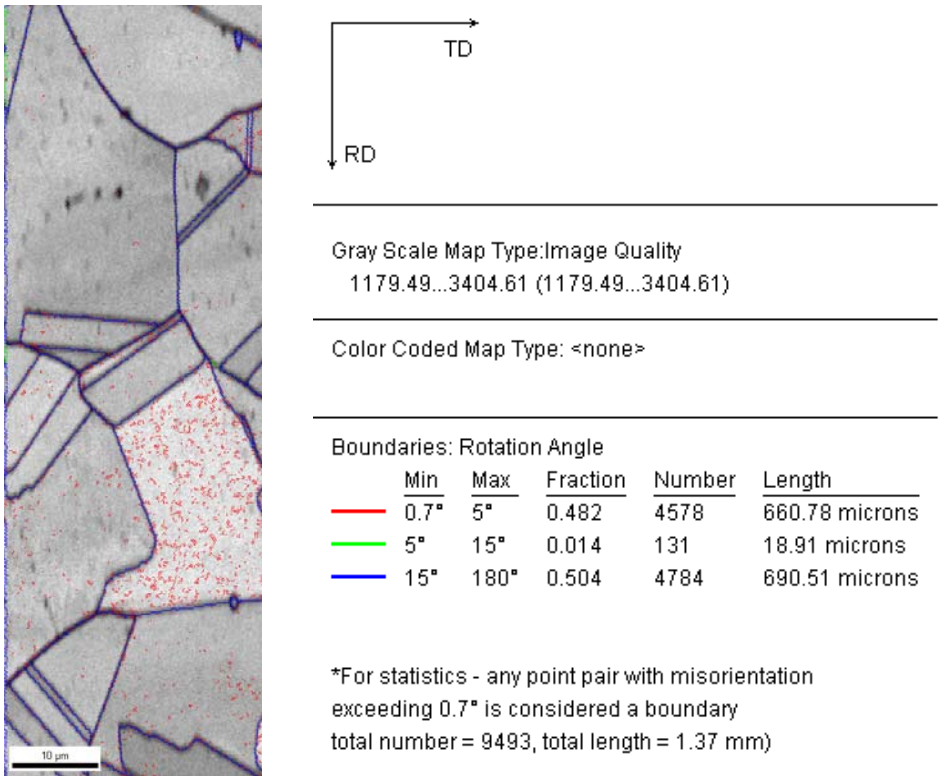

Figure 4- 11 Grain boundary map for base metal from the FSW 304L plate. The map shows large statically recrystallized grains.

A grain boundary map for the advancing side of the stir zone in one of the weld samples is shown on the next page in Figure 4-12. As the key to the grain boundary map indicates, the dislocation cell boundaries (0.7-5.0° boundaries) are highlighted red, the low angle boundaries (5.0-15.0° boundaries) are highlighted green, and the high angle boundaries (15.0-180.0° boundaries) are highlighted blue. The grain boundary map shows dislocation cell boundaries and low angle boundaries inside of larger high angle boundary grains. This indicates that the larger grains have undergone deformation, which was in part stored in the lattice as strain energy. The grain boundary maps for the other weld samples produced results similar to those shown in Figure 4-12. The data in the key of the grain boundary map was used to calculate the fraction of cell boundaries (Equation 3-1). The conclusion that only DRV and CDRX are the EPM considered active in FSW

of 304L is supported by the presence of dislocation cells and low angle boundaries in the grain boundary map.

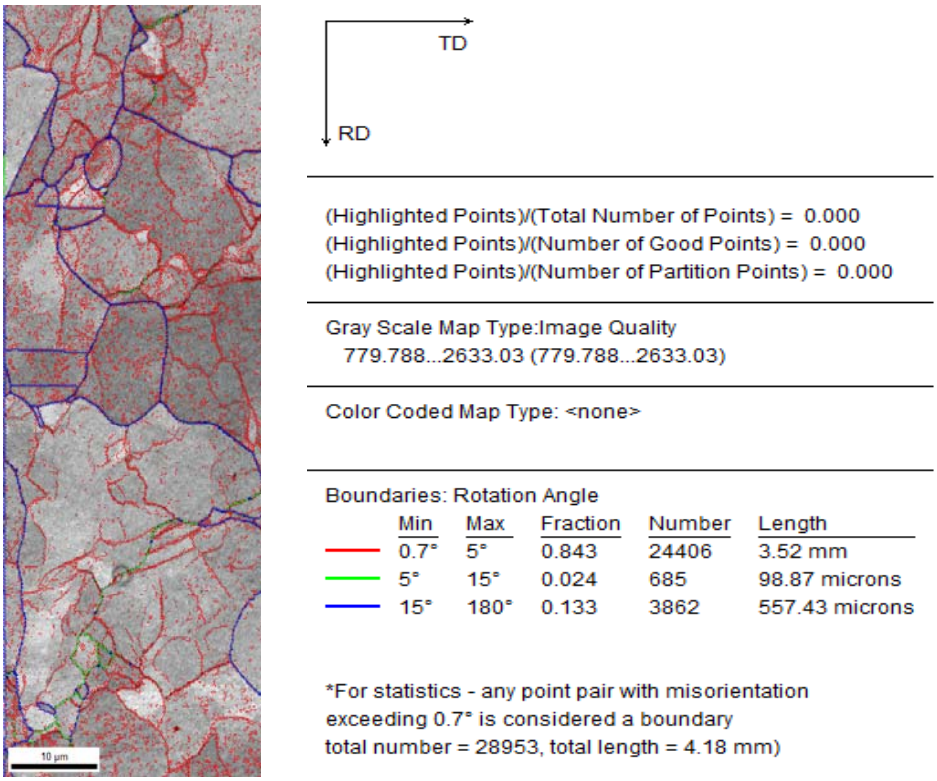

Figure 4- 12 Grain boundary map for the advancing side of the stir zone in one of the weld samples. The map shows deformed grains filled with dislocation cells. The grain boundary maps for the other weld samples produced similar results.

4.3.3 Models of Stir Zone EBSD Data

The results and discussion of regression analyses on stir zone data are presented in this section. The full details of the analyses can be found in Appendix F. A coefficient plot for the regression analysis using the spindle speed (SS), travel speed (TS), and location in stir zone (LSZ) basis is shown in Figure 4-13. The red dashed line represents

the critical coefficient size below which a coefficient becomes statistically insignificant. The intercept value, TS, and LSZ were the only significant factors in the analysis.

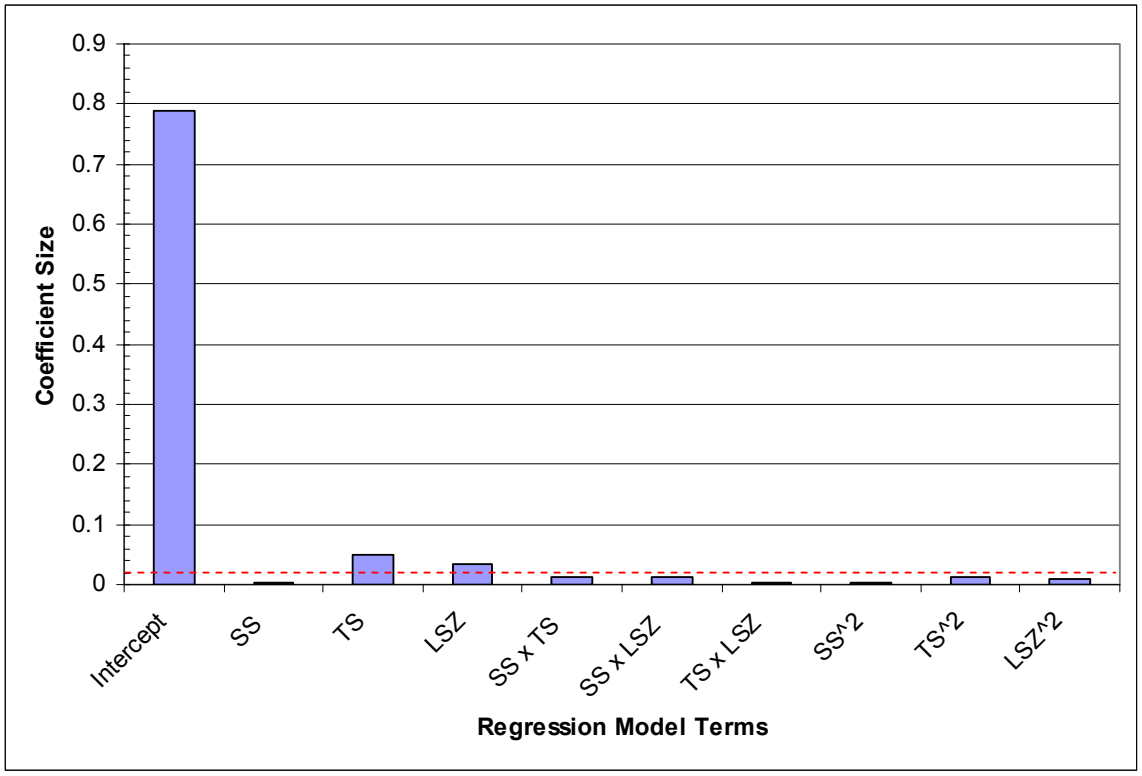

Figure 4- 13 Coefficient plot for regression analysis on stir zone data using the spindle speed (SS), travel speed (TS), and location in stir zone (LSZ) basis. The red dashed line represents the critical coefficient size below which a coefficient becomes statistically insignificant. The intercept, TS, and LSZ were the only significant factors.

After one at a time backward elimination, the final model of the fraction of cell boundaries in the stir zone microstructure is shown in Equation 4-1. The factors SS and LSZ in the equation are input as coded values.

$$\text{Fraction of Cell Boundaries}_{\text{Predicted}} = 0.771 - 0.049\text{TS} + 0.035\text{LSZ} \qquad (4\text{-}1)$$

The contour plot for Equation 4-1 is shown in Figure 4-14. The plot shows approximately 20% or less predicted change in fraction of cell boundaries across the experimental space.

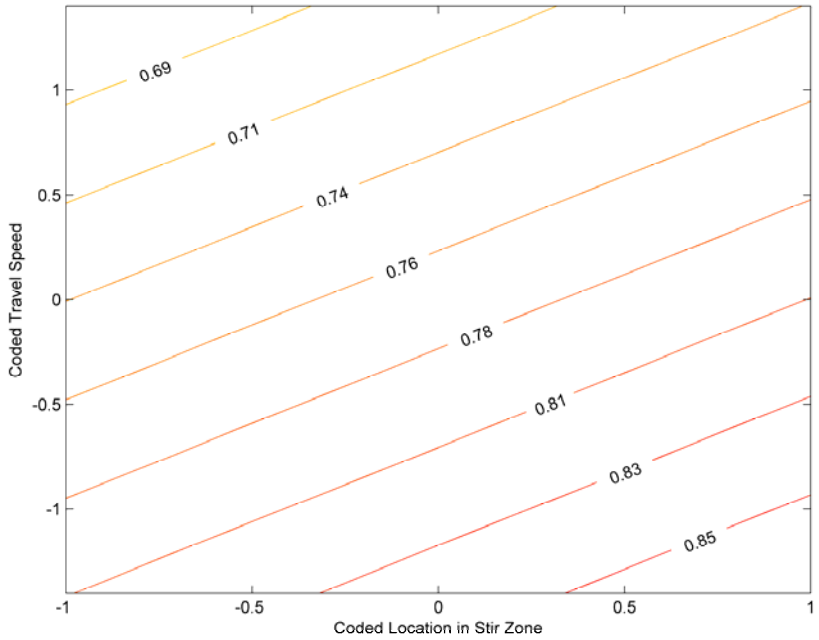

Figure 4- 14 Contour plot for Equation 4-1. Plot shows approximately 20% or less predicted change in fraction of cell boundaries across the experimental space.

A coefficient plot for the regression analysis using the θ-α-LSZ basis is shown in Figure 4-15. The intercept value, θ, α, and LSZ were the only significant factors. After one at a time backward elimination, the final model of the fraction of cell boundaries in the stir zone microstructure is shown in Equation 4-2. The factors θ, α, and LSZ in the equation are input as coded values.

$$\text{Fraction of Cell Boundaries}_{\text{Predicted}} = 0.771 + 0.033\theta - 0.036\alpha + 0.035\text{LSZ} \quad (4\text{-}2)$$

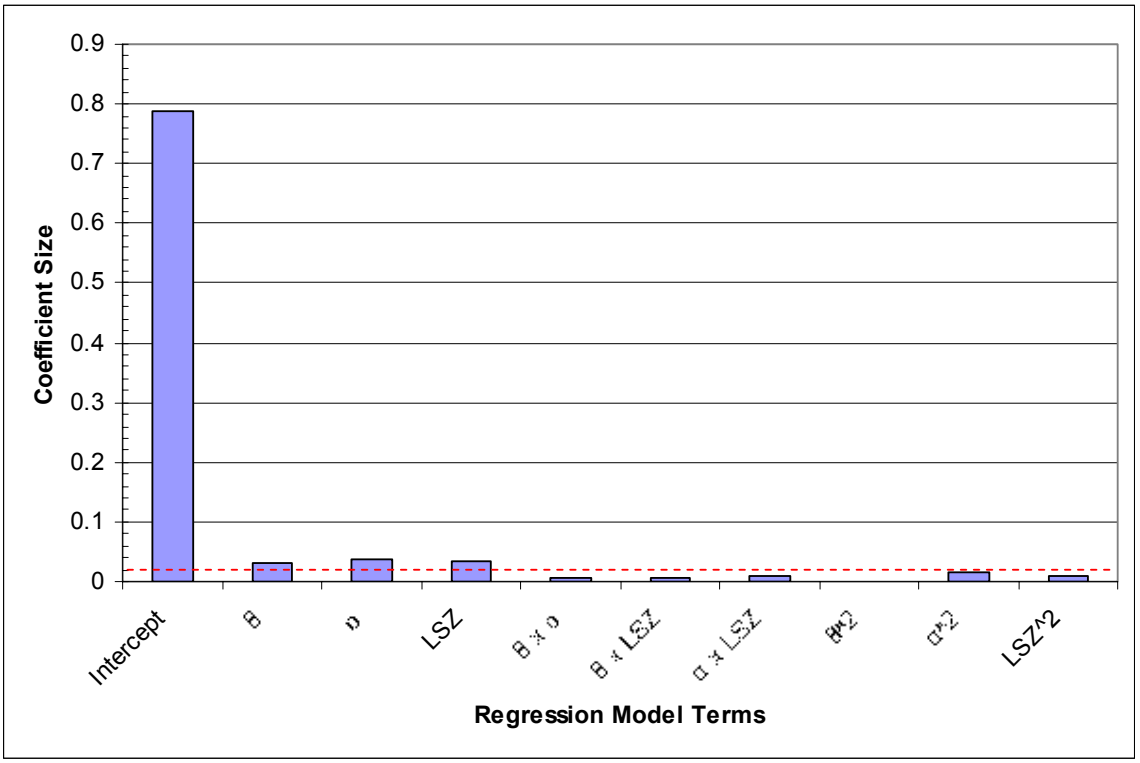

Figure 4- 15 Coefficient plot for the regression analysis on stir zone data using the θ-α-LSZ basis. The red dashed line represents the critical coefficient size below which a coefficient becomes statistically insignificant. The intercept, θ, α, and LSZ were the only significant factors.

The contour plots for the Equation 4-2 model are shown in Figures 4-16, 4-17, and 4-18. Figure 4-16 is the α-LSZ plot which shows approximately 15% or less predicted change in fraction of cell boundaries across the experimental space. Figure 4-17 is the θ-LSZ plot which also shows approximately 15% or less predicted change in fraction of cell boundaries across the experimental space. Figure 4-18 is the θ-α plot which shows approximately 15% or less predicted change in fraction of cell boundaries across the experimental space.

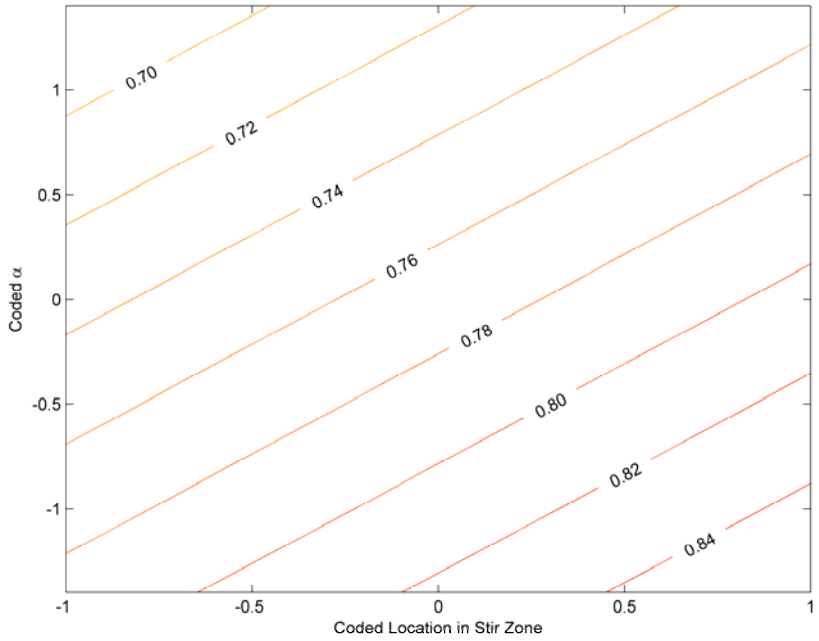

Figure 4- 16 α-LSZ contour plot for Equation 4-2. Plot shows approximately 15% or less predicted change in fraction of cell boundaries across the experimental space.

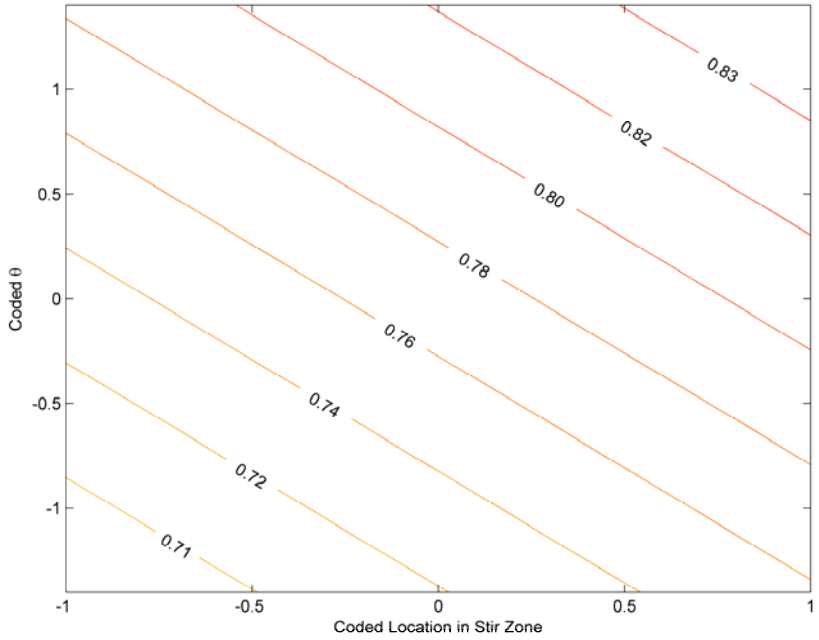

Figure 4- 17 θ-LSZ contour plot for Equation 4-2. Plot shows approximately 15% or less predicted change in fraction of cell boundaries across the experimental space.

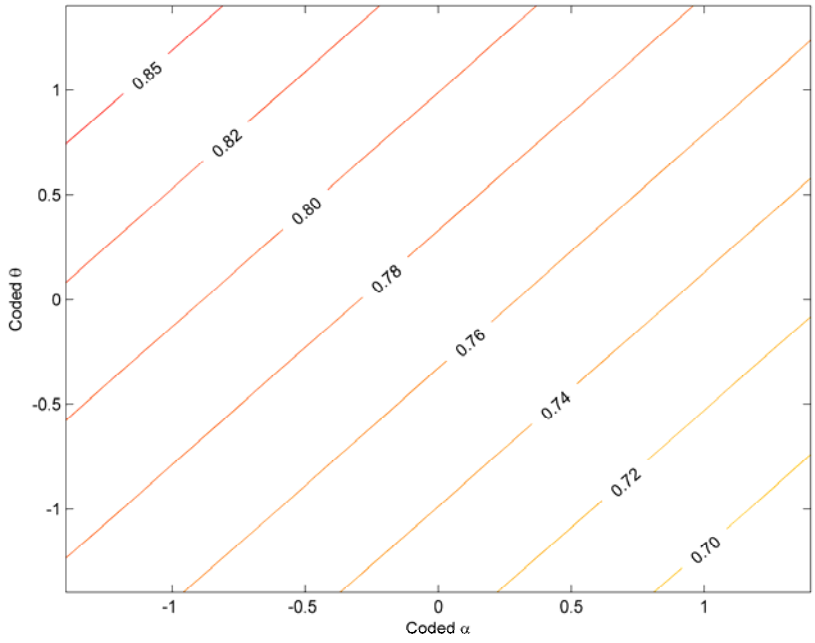

Figure 4- 18 θ-α contour plot for Equation 4-2. Plot shows approximately 15% or less predicted change in fraction of cell boundaries across the experimental space.

The gage capability study on the EBSD data collection and analysis process (see Appendix E) showed that the smallest effect on fraction of cell boundaries that the process can measure is 0.021. All of the effect sizes in the models (effect =2*coefficient) are at least 3 times larger the smallest measurable effect. This indicates that the regression analyses have detected real signal in the data rather random changes in the data due to measurement error.

Furthermore, the regression analyses indicate that the factors in the final models (Equations 4-1 and 4-2) are statistically significant. However, the contour plots (less than 20% change) indicate that the effects that these factors have on the fraction of cell boundaries are not practically significant. To explain this, recall that an increase in the fraction of cell boundaries suggests that the occurrence of DRV is increasing and that a

decrease in the fraction of cell boundaries suggests that the occurrence of CDRX is increasing. If CDRX became far more dominant than DRV, then the fraction of cell boundaries would decrease significantly. This is because the presence of dislocation cell boundaries would decrease due to CDRX causing cell boundaries to evolve to low angle and high angle misorientation boundaries.

The fraction of cell boundaries predicted by the stir zone models are relatively high and there is no large decrease in fraction of cell boundaries. Consequently, from the relatively high predicted fraction of cell boundaries it can be concluded that in the stir zone DRV dominates and limited CDRX occurs. This is confirmed by the EBSD grain boundary map which show an abundance of dislocation cells formed by DRV and high angle boundaries and limited low angle boundaries formed by CDRX. From the fact that there is no large decrease in predicted fraction cell boundaries it can be concluded that changes in occurrence of DRV and CDRX are not practically significant. Or in other words, the effects that the regression analysis factors have on the fraction of cell boundaries are not practically significant.

A comparison of the coefficients of the fraction of cell boundaries model in Equation 4-1 with the coefficients of the fraction of cell boundaries model in Equation 4-2 verified that the two different regression analyses resulted in the same model (see Appendix G). This suggests that the alternate θ-α-LSZ basis provides a valid method for relating the tool temperature to spindle speed and travel speed.

Figure 4-19 shows the SS-TS and θ-α bases overlaid, relative to each other. Along with the bases, the tool temperature contours and the experimentally measured tool temperatures, which correspond to the weld parameters in the central composite design,

are shown in the figure. The tool temperature contours agree with the experimental points, although the residual errors at the (0, -1.414), (1, -1), and (-1, 1) locations are roughly 3-5 times larger than the residual errors at the other points. The vector θ points in the direction of the tool temperature gradient, while the vector α parallel to the tool temperature isotherms. This indicates that all combinations of (SS, TS) that lie on the vector α should be constant tool temperature.

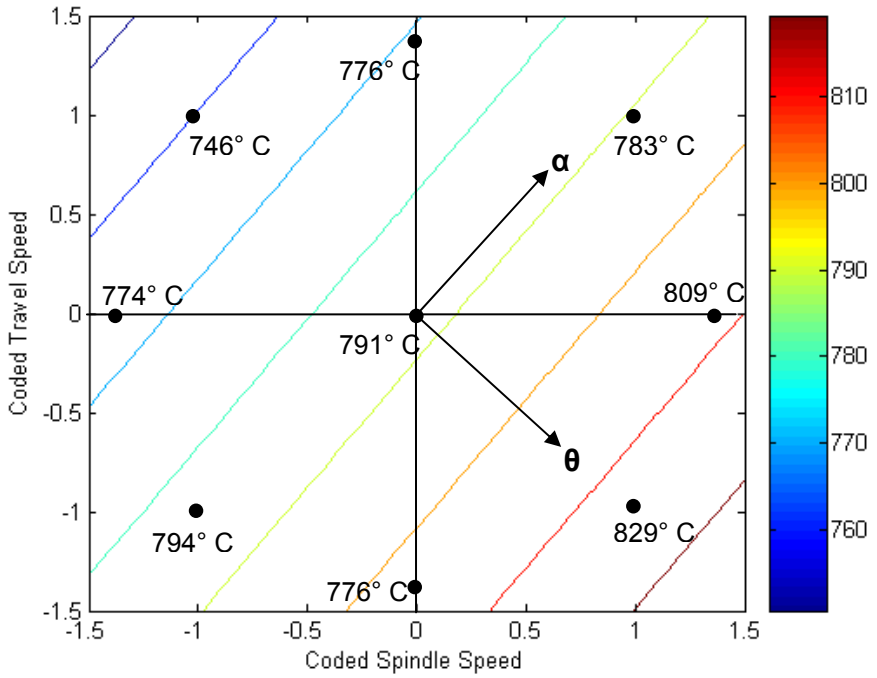

Figure 4- 19 Spindle speed-travel speed (SS-TS) and θ-α bases overlaid, relative to each other, on the tool temperature contours and data. The figure shows the experimentally measured tool temperatures that correspond to the weld parameters in the central composite design. The tool temperature contours agree with the experimental points, although the residual error at the (0, -1.414), (1, -1), and (-1, 1) locations is slightly larger than the residual error at the other points. The vector θ points in the direction of the tool temperature gradient, while the vector α is parallel to the tool temperature isotherms. Consequently, all combinations of (SS, TS) that lie on α are constant tool temperature.

4.3.4 Models of Thermo-Mechanically Affected Zone EBSD Data

The results and discussion of regression analyses on TMAZ data are presented in this section. The full details of the analyses can be found in Appendix H. A coefficient plot for the regression analysis using the spindle speed and travel speed (SS-TS) basis is shown in Figure 4-20. The plot shows that the intercept value and TS were the only significant factors in the analysis.

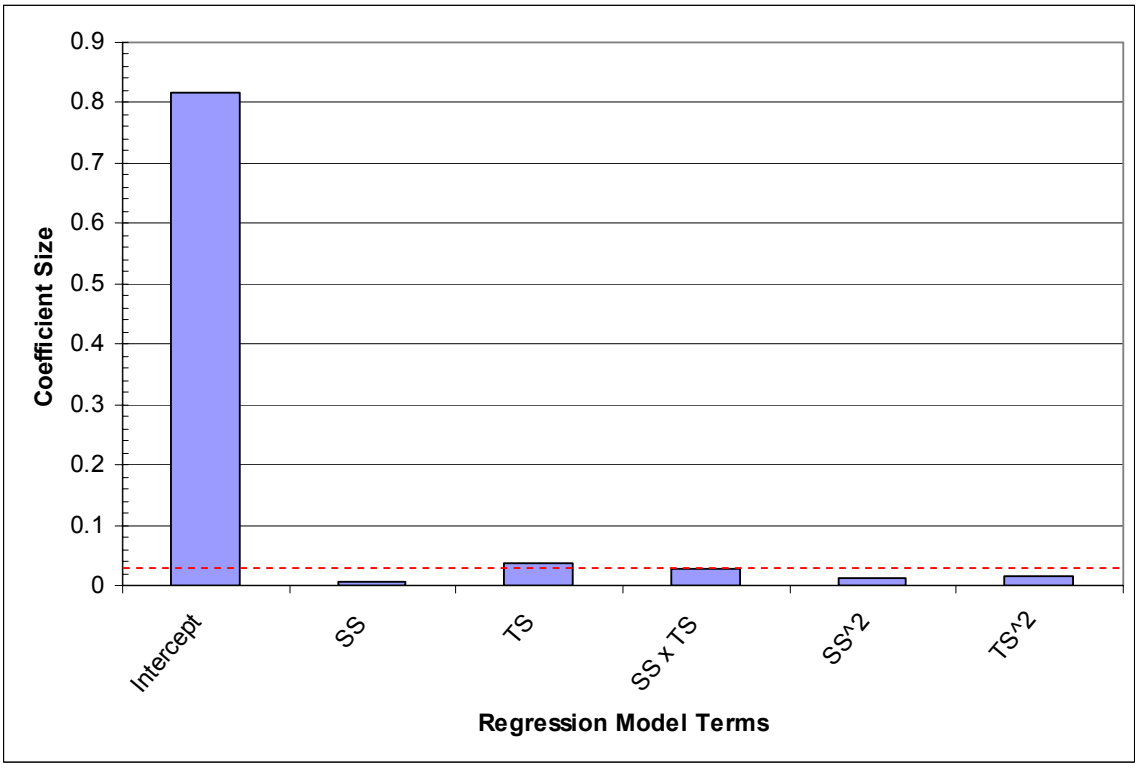

Figure 4- 20 Coefficient plot for the regression analysis on TMAZ data using the spindle speed and travel speed (SS-TS) basis. The red dashed line represents the critical coefficient size below which a coefficient becomes statistically insignificant. The intercept and TS were the only significant factors.

After one at a time backward elimination the final TMAZ model using the spindle speed and travel speed (SS-TS) basis is shown in Equation 4-3. The factor TS in the equation is input in coded values.

$$\text{Fraction of Cell Boundaries}_{\text{Predicted}} = 0.795 - 0.038\text{TS} \qquad (4\text{-}3)$$

The response plot for Equation 4-3 is shown in Figure 4-21. It shows approximately 10% predicted change in fraction of cell boundaries across the experimental space.

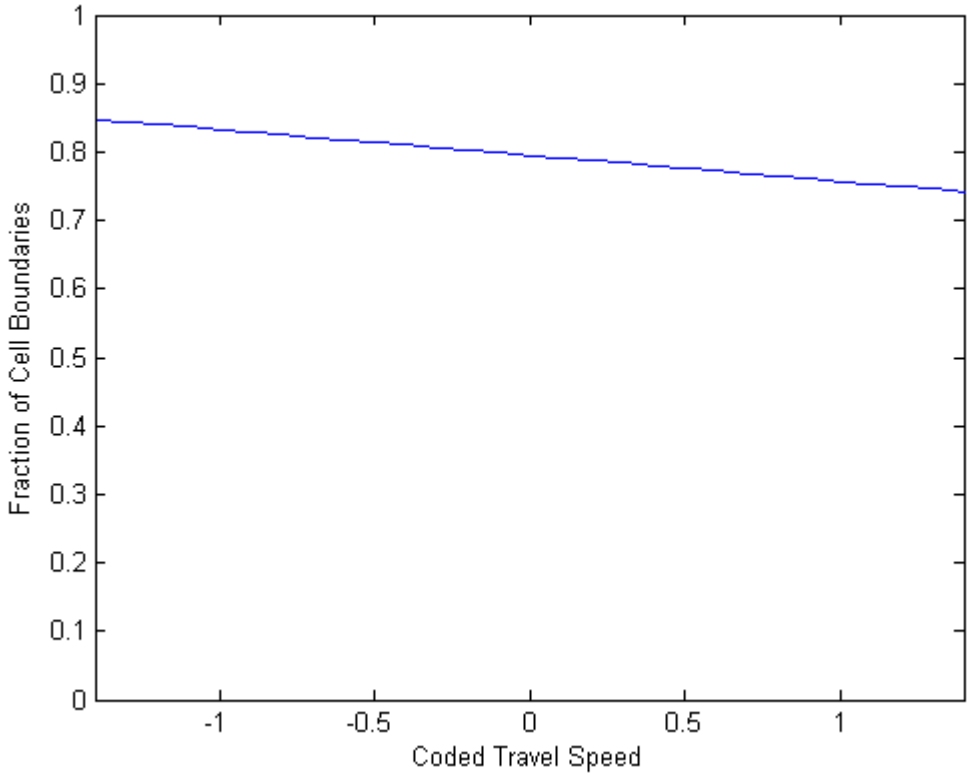

Figure 4- 21 Travel speed response plot for Equation 4-3. Plot shows approximately 10% predicted change in fraction of cell boundaries across the experimental space.

A coefficient plot for the regression analysis using the θ-α basis is shown in Figure 4-22. The plot shows that the intercept value, α, and α^2 are the only significant factors in the analysis, θ is marginally significant.

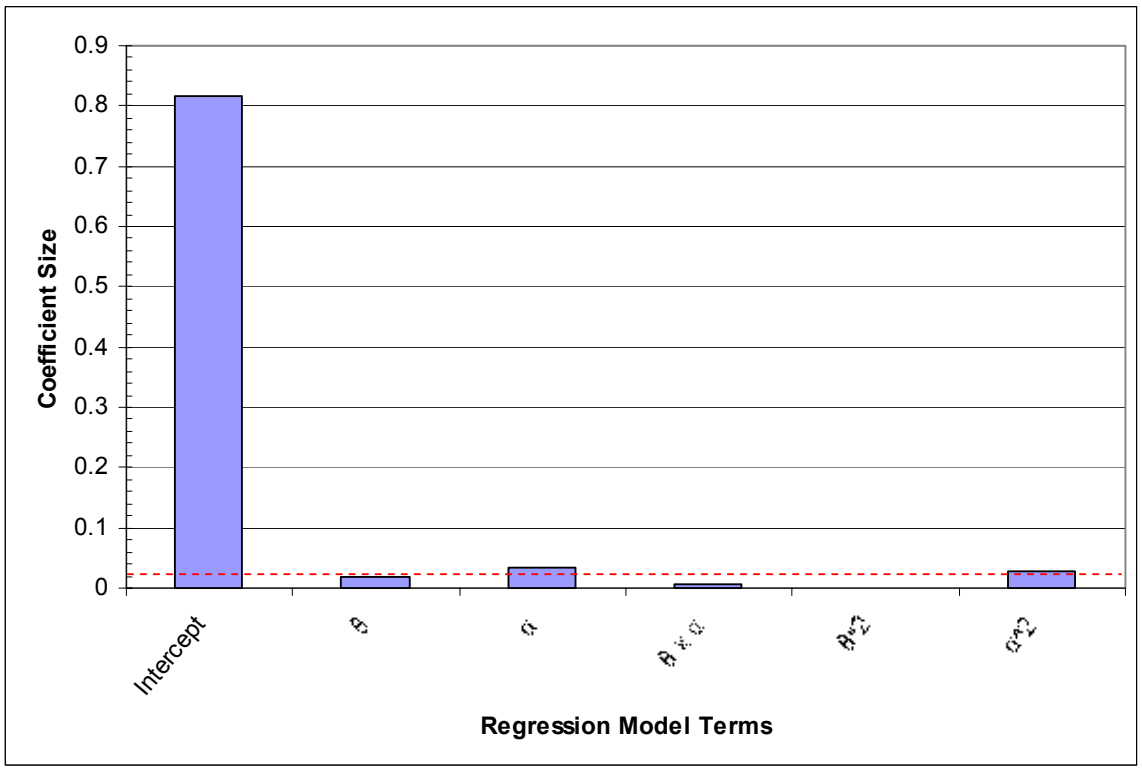

Figure 4- 22 Coefficient plot for the TMAZ regression model using the θ-α basis. It shows that the intercept, α, and α2 are the only significant factors in the analysis.

After one at a time backward elimination θ became significant resulting in the final TMAZ model shown in Equation 4-4. The factors θ, α, and α^2 in the equation are input as coded values.

$$\text{Fraction of Cell Boundaries}_{\text{Predicted}} = 0.815 + 0.018\theta - 0.033\alpha - 0.027\alpha^2 \qquad (4\text{-}4)$$

The θ-α contour plot for the model in Equation 4-4 is shown in Figure 4-23. Figure 4-23 shows approximately 10% predicted change in fraction of cell boundaries across the experimental space.

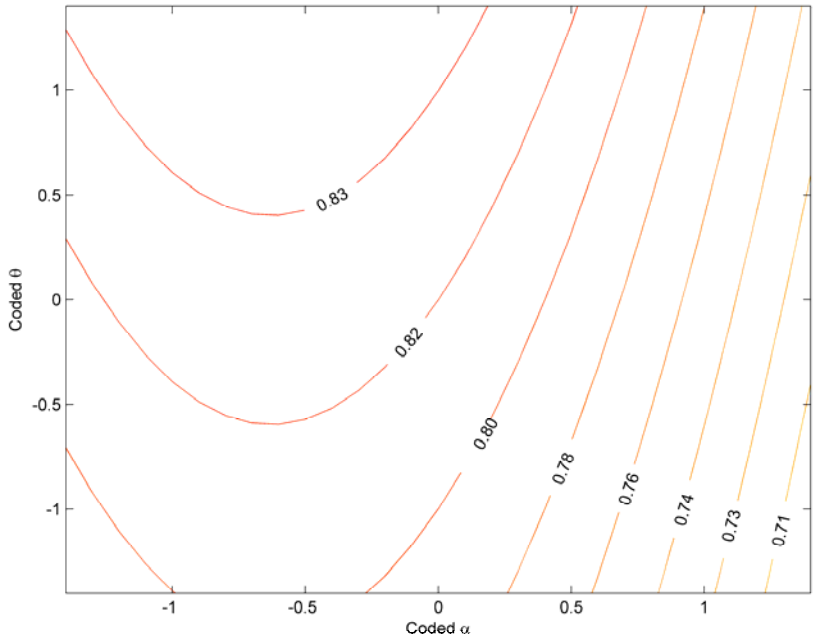

Figure 4- 23 θ-α contour plot for Equation 4-4. Plot shows approximately 10% predicted change in fraction of cell boundaries across the experimental space.

Comparing the models in Equations 4-3 and 4-4 to the results of the gage capability study (see Appendix E) indicates that all of the effects sizes in the models are larger than smallest measurable effect (0.021). However, the size of the effect of θ (0.036) is close enough to smallest measureable effect to cast doubt on the significance of θ. Furthermore, although the factors in the models are all statistically significant, the 10% or less change in the contour plots suggests that the factors are not practically significant. Additionally, the magnitude of the curvature shown in Figure 4-23 suggests

that α^2 is not practically significant. Furthermore, from the relatively high predicted fraction of cell boundaries it can be concluded that in the TMAZ DRV dominates and limited CDRX occurs.

The models in Equations 4-3 and 4-4 were of different orders. Consequently, the models' coefficients could not be compared as they were in the case of models of stir zone data. A substitution process was utilized in order to compare the models (see Appendix I). In Chapter 3, a process was used to find an alternate θ-α basis (see Appendix D). This process produced expressions for θ and α, both of which were in terms of spindle speed and travel speed. As seen in Equation 4-5, these expressions for θ and α were substituted into Equation 4-4, which produced an expression for Equation 4-4 in terms of spindle speed (SS) and travel speed (TS).

$$\begin{aligned}&\text{Fraction of Cell Boundaries}_{\text{Predicted}}\\&= 0.815 - 0.006\text{SS} - 0.037\text{TS} - 0.026\text{SS x TS} - 0.010\text{SS}^2 - 0.017\text{TS}^2\end{aligned} \tag{4-5}$$

Comparing the sizes of the effects in Equation 4-5 to the results of the gage capability casts doubt on the effects of SS, SS^2, TS^2, and possibly the SS x TS interaction.

The percent difference between each prediction by Equations 4-3 (f_2) and 4-5 (f_1) was calculated by comparing the difference in predictions to the average prediction, as shown in Equation 4-6.

$$\%\ \text{Difference in Model Predictions} = \frac{f_1 - f_2}{\left(\frac{f_1 + f_2}{2}\right)} \text{x } 100 \tag{4-6}$$

Figure 4-24 shows a contour plot of the percent difference in model predictions. The contour plot shows a minimum -11% difference and maximum of 6% difference. Although the models are of different orders, the relatively small percent differences in

predictions suggest that the models' predictive capabilities are similar. Furthermore, the locations of the contour plot that exceed ±6% difference in predictions technically lie outside the central composite design experimental space.

Equation 4-7 is obtained by removing the factors from Equation 4-5 whose effect sizes are close to the measurable limit. Removing the SS x TS interaction from Equation 4-7 would make the equation even more similar to Equation 4-3. From these results it can be concluded that the regression analyses of the two different bases (SS-TS and θ-α) essentially produced the same model where only the travel speed is significant.

$$\text{Fraction of Cell Boundaries}_{\text{Predicted}} = 0.815 - 0.037\text{TS} - 0.026\text{SS x TS} \qquad (4\text{-}7)$$

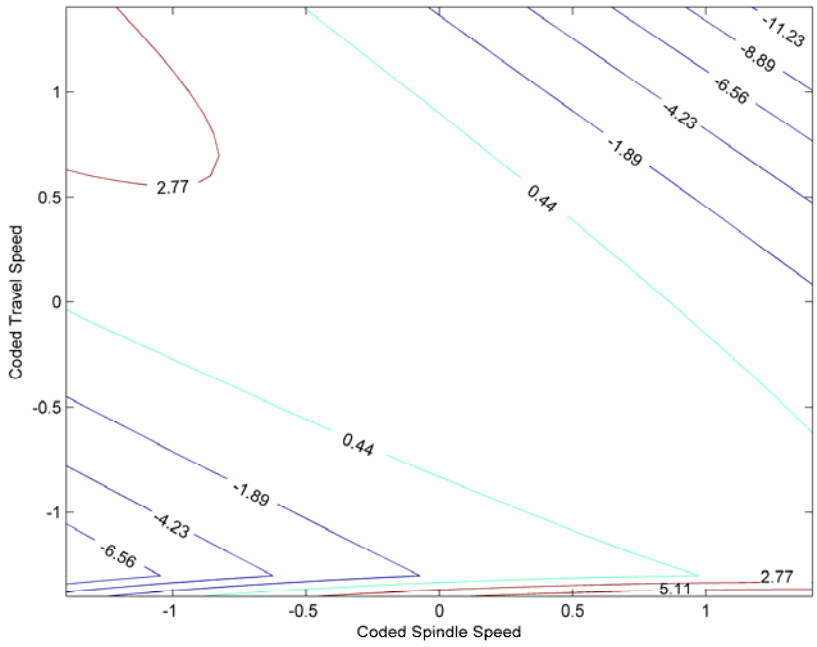

Figure 4- 24 Percent difference between fraction of cell boundaries model predictions (see Equation 4-6). The surface plot shows a minimum -11% difference and maximum 6% difference. Although the models are of different orders, the relatively small percent differences in predictions suggest that the models' predictive capabilities are similar.

By verifying that the dimensionally equivalent alternate θ-α basis produces approximately the same models as the SS-TS basis, it suggests that the alternate basis provides a valid method for relating the tool temperature to spindle speed and travel speed. Appendix D contains Equation D-4 which is an expression for the normalized vector α. Recall that all combinations of (SS, TS) which lie on the vector α should be constant tool temperature. Using the coefficients for SS and TS in Equation D-4, a constant tool temperature weld pitch, Φ, can be determined by a ratio of coefficients, as shown in Equation 4-8.

$$\Phi = \frac{TS_{Coded}}{SS_{Coded}} = \frac{0.791}{0.612} = 1.292 \tag{4-8}$$

Expressions for the coded spindle speed (SS_{Coded}) and travel speed (TS_{Coded}) are shown in Equation 4-9 and 4-10, respectively. Equations 4-9 and 4-10 were used to code the spindle speed and travel speed values in Appendix C. In the Equations, SS, TS, center point values, and the range value are all input as actual factor values, not coded values.

$$SS_{Coded} = \frac{(SS - \text{Center Point Value})}{\frac{\text{Range}}{2}} \tag{4-9}$$

$$TS_{Coded} = \frac{(TS - \text{Center Point Value})}{\frac{\text{Range}}{2}} \tag{4-10}$$

Substituting Equations 4-9 and 4-10 into Equation 4-8 yields Equation 4-11 which is an expression for a constant tool temperature weld pitch in terms of actual spindle speed and travel speed.

$$\Phi = 1.292 = \frac{(TS - 4)}{(SS - 400)} 50 \tag{4-11}$$

However, Equation 4-11 is too general to be practically useful because there are infinitely many combinations of SS and TS that satisfy the expression. Another equation is required in order to make Equation 4-11 more useful. Equation 4-12 provides the additional equation. Consider the case where a weld is run using a spindle speed (SS_0) and travel speed (TS_0), which results in a desirable tool temperature. In order to maintain that desirable tool temperature while changing the parameters to a new spindle speed (SS) and travel speed (TS), the ratio of the difference in travel speed over the difference in spindle speed would have to be equal to Φ, the constant tool temperature weld pitch, as shown in Equation 4-12.

$$\frac{TS - TS_0}{SS - SS_0} = \Phi \tag{4-12}$$

Setting Equations 4-11 and 4-12 equal, and solving for travel speed (TS) results in Equation 4-13. This expression can be used in the following manner. Suppose a given spindle speed (SS_0) and travel speed (TS_0) result in a desirable tool temperature for a weld. A new spindle speed (SS) can be selected and Equation 4-13 predicts what new travel speed (TS) should be used in order to maintain the desirable tool temperature.

$$TS = \frac{TS_0(SS - 400) - 200(SS + SS_0)}{50SS_0 - 49SS - 400} \tag{4-13}$$

5 CONCLUSIONS

In this study the EPM artifacts in the microstructure of 304L were characterized. First, in a cell structure investigation EBSD was used to characterize the EPM artifacts in material that was cold rolled and post-work heat-treated, and material that was hot torsion tested. Additionally, EBSD data collection and analysis was used with a DOE approach to model EPM artifacts in the final microstructure of FSW 304L. The conclusions of the study are presented below.

- There is evidence of well defined dislocations cells in 304L that has been hot torsion tested. However, there is a lack of dislocation cells in 304L that has been cold rolled and heat-treated. This suggests differences in dislocation mobility in the two deformation processes. More specifically, it suggests that dislocation cell formation requires the simultaneous operation of dislocation glide and climb, supporting the results of Kim et al. [21]. Results suggest that in 304L this condition only occurs during hot deformation.
- The gage capability study found that 0.021 was the magnitude of the smallest effect on the fraction of cell boundaries (see Equation 3-1) that the EBSD data collection and analysis process could detect. Good judgment should be used when a regression analysis reports an effect on

fraction of cell boundaries, whose magnitude is less than 0.021. This is because one can not be sure whether such an effect was actually caused by a change in a factor setting or is simply due to random variation in the measurement process.

- The shear deformation texture makes up more than 88% of the texture detected in FSW 304L. This indicates that not all EPM considered in this thesis are active in FSW 304L. Only DRV and CDRX are active in producing EPM artifacts in the final microstructure, while DDRX is not.
- Regression analyses of EBSD data from FSW 304L indicate that the predicted fraction of cell boundaries were relatively high (approximately 0.70 or more) and changed by 20% or less in the stir zone microstructure and 10% or less in the TMAZ. The relatively high fraction of cell boundaries means that in FSW of 304L DRV dominates and limited CDRX occurs. The small changes in predicted fraction of cell boundaries across the experimental space means that changes in the roles of DRV and CDRX are not practically significant.
- The alternate tool temperature basis provides a valid method for relating tool temperature to spindle speed and travel speed. More specifically, Equation 4-13 gives an expression for selecting multiple combinations of spindle speeds and travel speeds such that a constant tool temperature should be maintained.

REFERENCES

1. Buffa, G and L Fratini, "Friction stir welding of steels: process design through continuum based FEM model", *Science and Technology of Welding and Joining*, vol. 14, no. 3, 239-246 (2009)

2. Heurtier, P, C Desrayaud, F Montheillet, "A Thermomechanical Analysis of the Friction Stir Welding Process", *Material Science Forum*, vol. 396-402, 1-6 (2002)

3. Heurtier, P, MJ Jones, C Desrayaud, JH Driver, F Montheillet, D Allehaux, "Mechanical and thermal modeling of Friction Stir Welding", *Journal of Materials Processing Technology*, vol. 171, 348-357 (2006)

4. Buffa, G, L Donati, L Fratini, L Tomesani, "Solid state bonding in extrusion and FSW: Process mechanics and analogies", *Journal of Materials Processing Technology*, vol. 177, 344-347 (2006)

5. Gerlich, A, G Avramovic-Cingara, TH North, "Stir Zone Microstructure and Strain Rate during Al 7075-T6 Friction Stir Spot Welding", *Metallurgical and Materials Transactions*, vol. 36A, no. 9, 2773-2786 (2006)

6. Zhang, Z and JT Chen, "The simulation of material behaviors in friction stir welding process by using rate-dependent constitutive model", *Journal of Materials Science*, vol. 43, no. 1, 222-232 (2008)

7. Park, SHC, YS Sato, H Kokawa, K Okamoto, S Hirano, M. Inagaki, "Rapid formation of the sigma phase in 304 stainless steel during friction stir welding", *Scripta Materialia*, vol. 49, no. 12, 1175-1180 (2003)

8. Lena, AJ and WE Curry, "The Effect of Cold Work and Recrystallization on the Formation of the Sigma Phase in Highly Stable Austenitic Stainless Steels", *Transactions of American Society for Metals*, vol. 47, 193-210 (1955)

9. "Recovery, Recrystallization, and Grain-Growth Structures", *ASM Handbook Volume 14A*, 552-562

10. Doherty, RD, DA Hughes, FJ Humphreys, JJ Jonas, D Juul Jensen, ME Kassner, WE King, TR McNelley, HJ McQueen, AD Rollett, "Current issues in

recrystallization: a review", *Materials Science and Engineering A*, vol. 238, 219-274 (1997)

11. "Polycrystal Modeling, Plastic Forming, and Deformation Textures", *ASM Handbook Volume 14A*, 671-683

12. "Transformation and Recrystallization Textures Associated with Steel Processing", *ASM Handbook Volume 14A*, 685-699

13. McQueen, HJ and H Mecking, "Hot Rolling Deformation and Recrystallization Textures in fcc Metals", *Zeitschrift für Metallkunde*, vol. 78, no. 5, 387-396 (1987)

14. Hu, H and S.R. Goodman, "Cube-Textured Stainless Steel and Some of Its Properties", *Materials Science and Engineering*, vol. 67, no. 2, 143-155 (1984)

15. Kumar, BR, B Mahato, NR Bandyopadhyay, DK Bhattacharya, "Comparison of rolling texture in low and medium stacking fault energy austenitic stainless steels", *Materials Science and Engineering A*, vol. 394, 296-301 (2005)

16. Hertzberg, RW, *Deformation and Fracture Mechanics of Engineering Materials*, ed. 4, 77-79, Hoboken NJ (1996)

17. Mataya, MC, EL Brown, MP Riendeau, "Effect of Hot Working on Structure and Strength of Type 304L Austenitic Stainless Steel", *Metallurgical Transactions A*, vol. 21A, no. 7, 1969-1987 (1990)

18. Smallman, RE, and RJ Bishop, *Modern Physical Metallurgy & Materials Engineering*, ed. 6, 99-102, Woburn MA (1999)

19. McQueen, HJ, "The Production and Utility of Recovered Dislocation Substructures", *Metallurgical Transactions A*, vol. 8A, no. 6, 807-824 (1977)

20. Hull, D, and DJ Bacon, *Introduction to Dislocations*, ed. 4, 52-55, Woburn MA (2001)

21. Kim, WY, S Hanada, T Takasugi, "Large Tensile Elongation Behavior of Fe-14 at% Si Single Crystal", *Acta Metallurgica*, vol. 46, no. 16, 5701-5713 (1998)

22. Sorensen, CD, TW Nelson, SM Packer, "Tool material for FSW high-temperature alloys", Proc. 3rd Int Sympo Friction Stir Welding TWI Kobe Japan CD-ROM (2001)

23. Reynolds, AP, W Tang, T Gnaupel-Harold, H Prask, "Structure, properties, and residual stress of 304L stainless steel friction stir welds", *Scripta Materialia*, vol. 48, 1289-1294 (2003)

24. Park, SHC, YS Sato, H Kokawa, K Okamoto, S Hirano, M Inagaki, "Corrosion resistance of friction stir welded 304 stainless steel", *Scripta Materialia*, vol. 51, no. 2, 101-105 (2004)

25. Park, SHC, YS Sato, H Kokawa, K Okamoto, S Hirano, M Inagaki, "Microstructural characterization of the stir zone containing residual ferrite in friction stir welded 304 austenitic stainless steel", *Science and Technology of Welding and Joining*, vol. 10, no. 5, 550-556 (2005)

26. Sato, YS, TW Nelson, CJ Sterling, "Recrystallization in type 304L stainless steel during friction stirring", *Acta Materialia*, vol. 53, 637-645 (2005)

27. Richard, V, R Chiron, P Gerber, M Gaspérini, B Bacroix, "Investigation of Dislocation Microstructures Formed in Heavily Deformed Metals Through the Combined Use of EBSD and TEM", *Advanced Engineering Materials*, vol. 5, no. 3, 161-165 (2003)

28. Humphries, FJ, "Review: Grain and subgrain characterization by electron backscatter diffraction", *Journal of Materials Science*, vol. 36, 3833-3854 (2001)

29. Montheillet, F, M Cohen, JJ Jonas, "Axial Stresses and Texture Development During the Torsion Testing of Al, Cu, and α-Fe", *Acta Metallurgica*, vol. 32, no. 11, 2077-2089 (1984)

30. Canova, GR, UF Kocks, JJ Jonas, "Theory of Torsion Texture Development", *Acta Metallurgica*, vol. 32, no. 2, 211-226 (1984)

31. Tóth, LS, P Gilormini, JJ Jonas, "Effect of Rate Sensitivity on the Stability of Torsion Textures", *Acta Metallurgica*, vol. 36, no. 12, 3077-3091 (1988)

32. Kocks, UF, CN Tomé, HR Wenk, *Texture and Anisotropy: Preferred Orientations in Polycrystals and their Effect in Materials Properties*, 187-191, Cambridge UK (1998)

33. Bocher, P, J Azar, BL Adams, JJ Jonas, "Using OIM to Interpret the Dynamically Recrystallized Texture of a Low Stacking Fault FCC Material", *Materials Science Forum*, vols. 273-275, 249-254 (1998)

34. Fonda, RW, and JF Bingert, "Texture variations in an aluminum friction stir weld", *Scripta Materialia*, vol. 55, 1052-1055 (2007)

35. Yutaka, SS, H Kokawa, K Ikeda, M Enomoto, S Jogan, T Hashimoto, "Microtexture in the Friction-Stir Weld of an Aluminum Alloy", *Metallurgical and Materials Transactions A*, vol. 32, no. 4, 941-948 (2001)

36. Chowdhury, SG, S Das, B Ravikumar, PK De, "Twinning-Induced Sluggish Evolution of Texture during Recrystallization in AISI 316L Stainless Steel After Cold Rolling", *Metallurgical and Materials Transactions A*, vol. 37, no. 8, 2349-2359 (2006)

37. Norton, S, *Ferrous Friction Stir Weld Physical Simulation*, Ohio State University, Columbus OH (2006)

38. Anton, H, and C Rorres, *Elementary Linear Algebra*, ed. 8, 298-305, New York NY (2000)

39. Nelder, JA, "The Selection of Terms in Response-Surface Models—How Strong is the Weak-Heredity Principle?", *The American Statistician*, vol. 52, no. 4, 315-318 (1998)

40. Peixoto, JL, "A Property of Well-Formulated Polynomial Regression Models", *The American Statistician*, vol. 44, no. 1, 26-30 (1990)

Appendix A. Machine Compliance Model

In this study machine compliance was measured. The motivation for this study is connected with past observation of discrepancies between machine depth and the depth reported by a dial indicator depth fitted to the tool holder. A weld was run in 304L with an initial machine depth of 0.160 in. The machine depth was increased by 0.002 in. every 1.5 in. of weld until a final depth of 0.180 in. was achieved.

The dial indicator depth was recorded after each machine depth change. From this, the difference between the machine depth and dial indicator depth (ΔZ) was calculated and plotted against the measured z force (lbf), making a machine compliance chart. As seen on the next page in Figure A-1, linear regression was used to fit a line to the machine compliance data. The expression shown in Figure A-1 indicates that the machine deflects 0.002 in. for every 1000 lbf in the z-direction. The non-zero y-intercept (0.0125 in.) indicates that the something else was deflecting in addition to the machine. It was determined that the additional deflection comes from gaps between the work piece and backing plates. In the case of this weld, 2 backing plates were used underneath the work piece, resulting in three interfaces. An estimated 0.004 to 0.005 in. gap per interface would explain the magnitude of the y-intercept. Conceptually, the work piece is loaded in compression as the tool engages the material, causing the plates to move closer together until the gaps at the interfaces are closed.

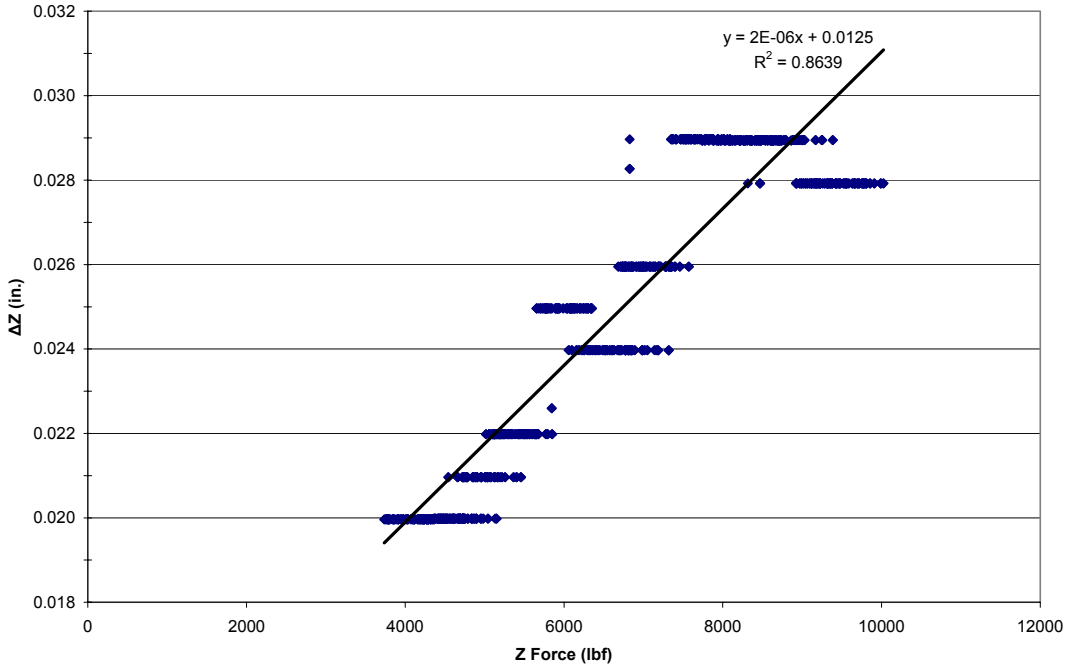

Figure A- 1 Machine compliance plot for FSW machine at BYU. Linear regression was used to fit a line to the compliance data. Expression indicates that the machine deflects 0.002 in. for 1000 lbf in the z-direction. The y-intercept represents the distance the work piece moves down under the force of the tool. This movement occurs because of the closure of gaps at the interfaces between the work piece and backing plates.

The expression obtained from the linear regression was used to correct the reported machine depth for each set of weld parameters. A spreadsheet that shows the corrected depth values, and the calculations used to obtain them, is shown on the next page in Table A-1. In the case of welds in the EPM in FSW study, one backing plate was used underneath the work piece. Consequently, the plate deflection was estimated as 0.01 in. As shown in the figure, the plate deflections and the calculated machine deflections were used with the reported machine depths to determine the corrected depth values.

Table A- 1 Spreadsheet that shows corrected weld depth values and the calculations used to determine them. The welds in the DOE study were run at a constant machine depth of 0.166 in. with one backing plate underneath the work piece. The plate deflection was estimated as 0.01 in. (0.005 in. gap per interface). The plate deflection and the calculated machine deflection were used with the reported machine depth to determine the corrected depth value.

Weld #	RPM	IPM	Z-Load (lbf)	Mach. Depth (in)	Plate Deflect. (in)	Mach. Compl. (in/lbf)	Mach. Deflection (in)	Corrected Depth (in)
1	400	1.172	11200	0.166	0.01	0.000002	0.0224	0.134
2	258.6	4	9200	0.166	0.01	0.000002	0.0184	0.138
3	300	2	11600	0.166	0.01	0.000002	0.0232	0.133
4	500	2	10500	0.166	0.01	0.000002	0.0210	0.135
5	400	4	9100	0.166	0.01	0.000002	0.0182	0.138
6	541.4	4	8200	0.166	0.01	0.000002	0.0164	0.140
7	300	6	10800	0.166	0.01	0.000002	0.0216	0.134
8	500	6	12000	0.166	0.01	0.000002	0.0240	0.132
9	400	6.828	10200	0.166	0.01	0.000002	0.0204	0.136

Appendix B. Rotations of EBSD Data and Rotated Textures

In order to perform the texture analyses the EBSD data sets were rotated to the shear deformation sample coordinate system. This was accomplished by rotating the data about the rolling direction (RD), transverse direction (TD), and normal direction (ND) in order to orient SPN-SD-XD sample coordinate system to that shown in the pole figures in Figure 2-1. The nominal rotation values (RD, TD, ND) for each location in the stir zone are as follows: retreating side (40°, -150°, 90°), weld center (40°, -150°, 0°), advancing side (40°, -150°, -90°), and TMAZ (40°, -150°, 90°). The actual rotation values are shown in Table B-1.

The textures used in the EBSD texture analysis are textures based on a torsional simple shear deformation sample coordinate system. However, the OIM Analysis software is based on a rolling deformation sample coordinate system. Consequently, the textures were rotated 90° about TD and 90° about ND in order to put them into the appropriate sample coordinate system for rolling deformation sample coordinate system software. The rotated Euler angles (radians) of the rotated cube texture and A, B, and C components of the shear deformation texture are shown below.

Rotated Cube Texture:

φ_1	Φ	φ_2
5.4978	0.0000	0.0000
0.7854	0.0000	0.0000
3.9270	0.0000	0.0000
2.3562	0.0000	0.0000

Table B- 1 Rotation angles (degrees) for orienting the SPN-SD-XD sample coordinate system to that of the 111 pole figures in Figure 2-1. The rotations were about RD, TD, and ND.

Advancing Rotation Order	**RD**	**TD**	**ND**
	3rd	2nd	1st
Weld Center Rotation Order	**RD**	**TD**	**ND**
	1st	2nd	3rd (if necessary)
Retreating Rotation Order	**RD**	**TD**	**ND**
	2nd	3rd	1st
TMAZ Rotation Order	**RD**	**TD**	**ND**
	2nd	3rd	1st

		RD (degrees)	TD (degrees)	ND (degrees)
1P	**Advancing**	22	170	-100
	Weld Center	20	150	0
	Retreating	45	163	107
	TMAZ	25	175	90
2P	**Advancing**	32	137	-80
	Weld Center	-40	128	-30
	Retreating	40	134	110
	TMAZ	23	160	107
3P	**Advancing**	44	120	-90
	Weld Center	-30	140	-32
	Retreating	40	130	95
	TMAZ	20	160	120
4P	**Advancing**	39	160	-69
	Weld Center	-17	167	14
	Retreating	33	170	107
	TMAZ	-5	134	100
5P (1)	**Advancing**	-5	180	-100
	Weld Center	-12	138	-12
	Retreating	40	140	100
	TMAZ	50	130	100
5P (2)	**Advancing**	-10	180	-100
	Weld Center	-15	135	-12
	Retreating	26	165	100
	TMAZ	50	130	100
5P (3)	**Advancing**	-5	180	-100
	Weld Center	-20	135	-18
	Retreating	25	165	100
	TMAZ	50	130	100
6P	**Advancing**	10	155	-100
	Weld Center	-20	130	-21
	Retreating	40	150	110
	TMAZ	57	155	112
7P	**Advancing**	27	130	-80
	Weld Center	-30	130	-20
	Retreating	25	165	115
	TMAZ	20	163	93
8P	**Advancing**	10	165	-105
	Weld Center	-25	138	-25
	Retreating	20	167	112
	TMAZ	55	165	120
9P	**Advancing**	14	130	-65
	Weld Center	-15	135	-5
	Retreating	35	140	88
	TMAZ	50	130	90

0.7854	3.1416	0.0000
5.4978	3.1416	0.0000
2.3562	3.1416	0.0000
3.9270	1.5708	0.0000
0.7854	1.5708	0.0000
5.4978	1.5708	0.0000
2.3562	1.5708	0.0000
3.9270	1.5708	0.0000
2.3562	1.5708	3.1416
3.9270	1.5708	3.1416
0.7854	1.5708	3.1416
5.4978	1.5708	1.5708
2.3562	1.5708	1.5708
3.9270	1.5708	1.5708
0.7854	1.5708	1.5708
5.4978	1.5708	1.5708
0.7854	1.5708	4.7124
5.4978	1.5708	4.7124
2.3562	1.5708	4.7124
3.9270	1.5708	4.7124

A Components:

φ_1	Φ	φ_2
2.18566	0.78584	3.14203
2.18566	2.35576	6.28275
0.95593	0.78583	6.28274
4.09753	2.35575	3.14203
0.61610	1.57080	5.49779
2.52550	1.57079	0.78540
2.52550	1.57079	3.92699
3.75770	1.57079	2.35619
2.18566	2.35576	1.57036
0.95594	2.35576	4.71283
2.18566	0.78584	4.71282
4.09753	0.78584	1.57036
1.57080	0.61610	3.92699
1.57080	2.52550	5.49779
1.57080	0.61610	5.49778
4.71239	0.61610	0.78540
2.45623	1.15045	2.67821
2.45623	1.99113	0.46339
2.45623	1.99113	3.60498
3.82696	1.99113	2.67821
2.45623	1.99113	2.03419
2.45623	1.15045	1.10742

2.45623	1.15045	4.24900
3.82696	1.15046	2.03418

B Components:

φ_1	Φ	φ_2
4.71239	2.18690	0.78540
4.71239	0.95470	0.78540
1.57080	0.95470	3.92699
2.61808	0.95582	2.35653
2.61808	2.18577	0.78507
2.61808	2.18577	3.92666
3.66510	2.18577	2.35653
2.61808	2.18577	2.35586
2.61808	0.95582	0.78574
2.61808	0.95582	3.92732
3.66510	0.95582	2.35586
3.66510	2.18577	5.49812
3.66510	0.95582	5.49745

C Component:

φ_1	Φ	φ_2
1.57080	1.57080	5.49779
1.57080	1.57080	3.92699
4.71239	1.57080	2.35619
4.71239	1.57079	0.78540
3.14160	2.35619	1.57080
3.14160	0.78540	1.57079
3.14160	0.78540	4.71238
1.57080	1.57080	3.92699
3.14160	0.78540	3.14159
3.14160	2.35619	3.14160
3.14160	2.35619	0.00000
3.14160	0.78540	6.28318

Appendix C. Regression Factors Matrix

The factors matrix used for the regression analysis is shown below in Table C-1. All factors used in the analysis are in coded form in the matrix. For the stir zone location factor, X3 = 1, X3 = 0, and X3 = -1 correspond to advancing side of the stir zone, stir zone center, and retreating of the stir zone, respectively.

Table C- 1 Factor matrix used for the regression analysis. All factors in the matrix are in coded form. For the stir zone location factor, X3 = 1, X3 = 0, and X3 = -1 correspond to advancing side of the stir zone, stir zone center (weld center), and retreating side of the stir zone, respectively.

		Spindle Speed	Travel Speed	Stir Zone Location	Interactions			Curvature		
Sample	Run	X1	X2	X_3	X1X2	X1X3	X2X3	X1^2	X2^2	X3^2
1P	1	0	-1.41	1.00	0	0	-1.414	0.000000	1.999396	1.00
2P	2	-1.41	0	1.00	0	-1.414	0	1.999396	0	1.00
3P	3	-1	-1	1.00	1	-1	-1	1.000000	1	1.00
4P	4	1	-1	1.00	-1	1	-1	1.000000	1	1.00
5P (1)	5	0	0	1.00	0	0	0	0.000000	0	1.00
5P (2)	6	0	0	1.00	0	0	0	0.000000	0	1.00
5P (3)	7	0	0	1.00	0	0	0	0.000000	0	1.00
6P	8	1.41	0	1.00	0	1.414	0	1.999396	0	1.00
7P	9	-1	1	1.00	-1	-1	1	1.000000	1	1.00
8P	10	1	1	1.00	1	1	1	1.000000	1	1.00
9P	11	0	1.41	1.00	0	0	1.414	0.000000	1.999396	1.00
1P	1	0	-1.41	0.00	0	0	0	0.000000	1.999396	0.00
2P	2	-1.41	0	0.00	0	0	0	1.999396	0	0.00
3P	3	-1	-1	0.00	1	0	0	1.000000	1	0.00
4P	4	1	-1	0.00	-1	0	0	1.000000	1	0.00
5P (1)	5	0	0	0.00	0	0	0	0.000000	0	0.00
5P (2)	6	0	0	0.00	0	0	0	0.000000	0	0.00
5P (3)	7	0	0	0.00	0	0	0	0.000000	0	0.00
6P	8	1.41	0	0.00	0	0	0	1.999396	0	0.00
7P	9	-1	1	0.00	-1	0	0	1.000000	1	0.00
8P	10	1	1	0.00	1	0	0	1.000000	1	0.00
9P	11	0	1.41	0.00	0	0	0	0.000000	1.999396	0.00
1P	1	0	-1.41	-1.00	0	0	1.414	0.000000	1.999396	1.00
2P	2	-1.41	0	-1.00	0	1.414	0	1.999396	0	1.00
3P	3	-1	-1	-1.00	1	1	1	1.000000	1	1.00
4P	4	1	-1	-1.00	-1	-1	1	1.000000	1	1.00
5P (1)	5	0	0	-1.00	0	0	0	0.000000	0	1.00
5P (2)	6	0	0	-1.00	0	0	0	0.000000	0	1.00
5P (3)	7	0	0	-1.00	0	0	0	0.000000	0	1.00
6P	8	1.41	0	-1.00	0	-1.414	0	1.999396	0	1.00
7P	9	-1	1	-1.00	-1	1	-1	1.000000	1	1.00
8P	10	1	1	-1.00	1	-1	-1	1.000000	1	1.00
9P	11	0	1.41	-1.00	0	0	-1.414	0.000000	1.999396	1.00

Appendix D. Alternate Tool Temperature Basis

This appendix outlines the process used to obtain an alternate tool temperature basis. First a regression analysis was carried out to determine the relationship between tool temperature and spindle speed (X1) and travel speed (X2). The results of that regression analysis are shown in Figure D-1. The tool temperature was transformed to coded values in order to make the regression analysis more accurate.

```
Predictor       Coef  SE Coef      T      P
Constant   -0.00548  0.09963  -0.05  0.958
SS          0.3660   0.1168    3.13  0.014
TS         -0.2832   0.1168   -2.42  0.042


S = 0.330421   R-Sq = 66.2%   R-Sq(adj) = 57.8%


Analysis of Variance

Source           DF      SS      MS     F      P
Regression        2  1.7128  0.8564  7.84  0.013
Residual Error    8  0.8734  0.1092
Total            10  2.5863
```

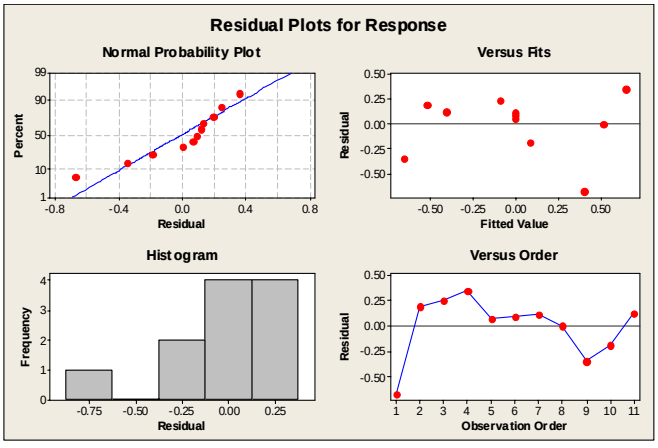

Figure D- 1 ANOVA table and residuals plots for tool temperature regression analysis.

The results of the regression analysis were used with the coded tool temperature data to form a vector θ, as shown in Equation D-1, such that is passed through the origin of the spindle speed-travel speed (SS-TS) basis.

$$\theta = T_{tool} - A_o = 0.366SS - 0.283TS \quad \text{(D- 1)}$$

where $A_o = 0.00548$ (regression intercept), T_{tool} is the coded tool temperature, and 0.366 and -0.283 are the spindle speed and travel speed coefficients, respectively.

The Gram-Schmidt process was used to find a vector α, shown in Equation D-2, which was orthogonal to the vector θ, forming an orthogonal basis.

$$\alpha = 0.375SS + 0.484TS \quad \text{(D- 2)}$$

The vectors θ and α were normalized, forming an orthonormal basis. The orthonormalized vectors θ and α are shown in Equations D-3 and D-4, respectively. The factors spindle speed and travel speed in the equations are input as coded values.

$$\theta_{Normalized} = 0.791SS - 0.612TS \quad \text{(D- 3)}$$

$$\alpha_{Normalized} = 0.612SS + 0.791TS \quad \text{(D- 4)}$$

Appendix E. Gage Capability Study

The gage capability study was carried out on six parts (as shown in Figure 7). The feature of the parts to be measured was the fraction of cell boundaries (see Equation 3-1). The gage to be used was EBSD data collection and analysis system. Three measurements of each part were taken by one operator (the author). The variation due to operator becomes confounded with the variation due to the gage, because only one operator was used. Consequently, the variations due to operator and gage were lumped together as one source of variation due to the measurement process, and variation due to the part was considered as a second source of variation. An ANOVA for two sources of variation was used to identify magnitudes of the variation due to the measurement process and the variation due to the part. The calculations for the ANOVA are shown in Table E-1. The $\sigma_{process}$ outlined in red is the smallest effect on fraction of cell boundaries than can be detected by the EBSD data collection and analysis process. It contains the variation due the operator and the variation due to the gage.

Table E- 1 ANOVA for two sources of variation. The σprocess outlined in red is the smallest effect on fraction of cell boundaries that can be detected by the EBSD data collection and analysis process. It contains the variation due to the operator and the variation due to the gage.

			Part									
		Trial	1	2	3	4	5	6				
Operator	A	a	0.7954	0.8008	0.8206	0.7679	0.8073	0.8517				
		b	0.8015	0.8217	0.8221	0.8141	0.8251	0.8210				
		c	0.8361	0.8299	0.8073	0.8400	0.8167	0.8143				

Anova: Single Factor

SUMMARY

Groups	*Count*	*Sum*	*Average*	*Variance*
1	3	2.43303	0.81101	0.00048
2	3	2.45236	0.81745	0.00022
3	3	2.45009	0.81670	0.00007
4	3	2.42199	0.80733	0.00133
5	3	2.44913	0.81638	0.00008
6	3	2.48705	0.82902	0.00040

ANOVA

Source of Variatio	*SS*	*df*	*MS*	*F*	*P-value*	*F crit*				
Between Groups	0.000815	5	0.000163	0.378796	0.853803	3.105875239	0.000163	$\sigma^2_E + r\sigma^2_P$	**r =**	3
Within Groups	0.005165	12	0.00043				0.00043	σ^2_E		
Total	0.00598	17								

Process	σ_E^2	0.000430385
Part	σ_P^2	-8.9119E-05
Total	σ_T^2	0.000341266

	$\sigma_{Process}$	0.021
	σ_{Part}	0.000
	σ_{Total}	0.018

← This variation is the smallest effect that can be detected by the EBSD data collection and analysis process. This contains the variation due to the operator and the variation due to the gage.

Appendix F. Regression Analyses of Stir Zone EBSD Data

The results of regression analyses of stir zone data are shown in this appendix. The analysis using the spindle speed (SS), travel speed (TS), and location in stir zone (LSZ) basis is shown in Figure F-1.

```
Predictor       Coef    SE Coef       T       P
Constant    0.771255   0.008102   95.20   0.000
TS         -0.048649   0.009501   -5.12   0.000
LSZ         0.034628   0.009923    3.49   0.002


S = 0.0465415   R-Sq = 56.1%   R-Sq(adj) = 53.2%


Analysis of Variance

Source           DF        SS        MS       F       P
Regression        2  0.083174  0.041587   19.20   0.000
Residual Error   30  0.064983  0.002166
Total            32  0.148157
```

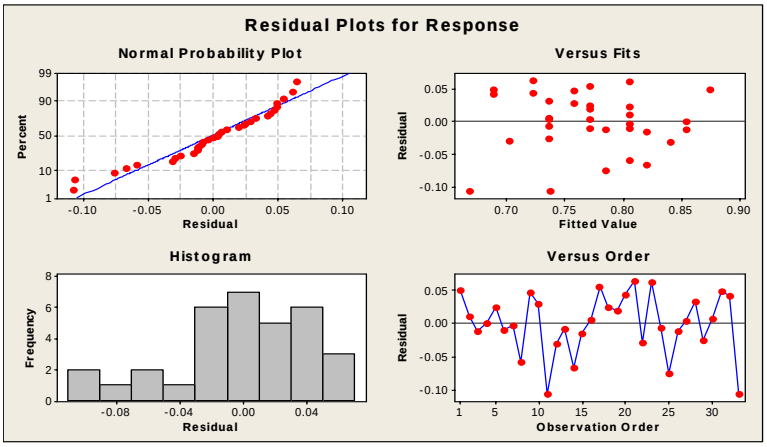

Figure F- 1 ANOVA table and residuals plots for regression analysis of stir zone data using the spindle speed (SS), travel speed (TS), and location in stir zone (LSZ) basis.

The analysis using the θ, α, and LSZ basis is shown in Figure F-2.

Predictor	Coef	SE Coef	T	P
Constant	0.771255	0.008222	93.81	0.000
θ	0.032525	0.009641	3.37	0.002
α	-0.036343	0.009641	-3.77	0.001
LSZ	0.03463	0.01007	3.44	0.002

S = 0.0472310 R-Sq = 56.3% R-Sq(adj) = 51.8%

Analysis of Variance

Source	DF	SS	MS	F	P
Regression	3	0.083465	0.027822	12.47	0.000
Residual Error	29	0.064692	0.002231		
Total	32	0.148157			

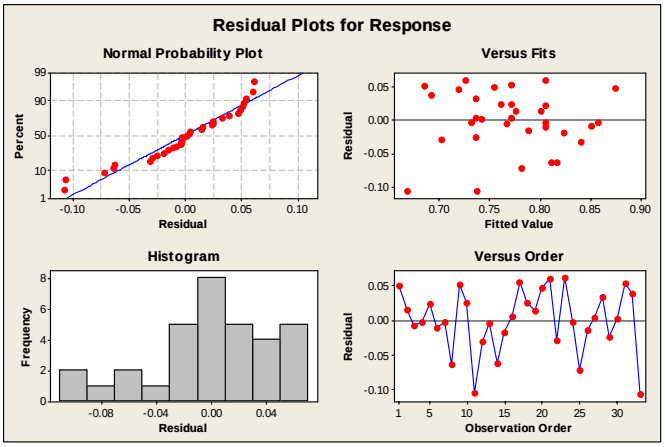

Figure F- 2 ANOVA table and residuals plots for regression analysis of stir zone data using the θ, α, and LSZ basis.

Appendix G. Coefficient Comparison of Models of Stir Zone Data

This appendix describes the process of comparing the models of the stir zone fraction of cell boundaries data by using the spindle speed-travel basis and the tool temperature (θ-α) basis. Figure G-1 shows the orientation of the two different models relative to the spindle speed-travel speed basis. The spindle speed-travel speed model is highlighted blue and the θ-α is highlighted red. The models were first compared vectorially relative to the spindle speed-travel speed basis. They were found to match each other within approximately 4°. The magnitudes of the model coefficients were also compared and were found to match identically. It can be concluded from the results of these comparisons that the models obtained are the same. This suggests the alternate tool temperature (θ-α) basis provides a valid method for comparing tool temperature to the fraction of cell boundaries in the stir zone data.

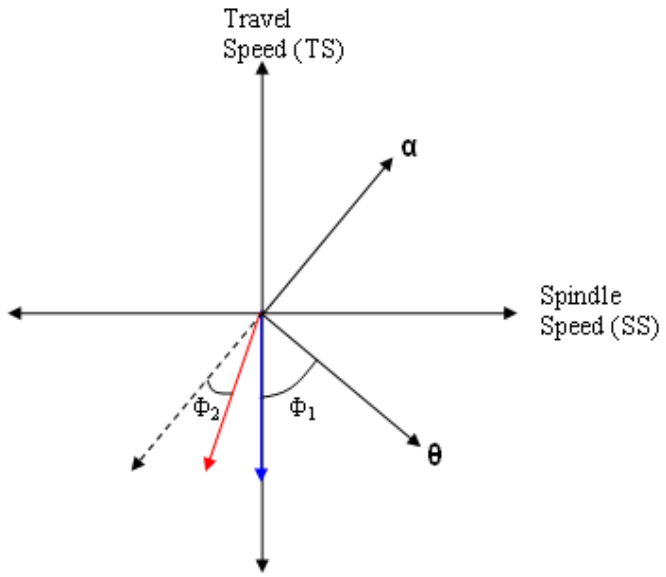

The tool temperature analysis determined the relationship between tool temperature and spindle speed (SS) and travel speed (TS), which resulted in the following expression.

$$\theta = 0.366SS - 0.283TS$$

The angle Φ_1 is defined by $\Phi_1 = \tan^{-1}(0.366/0.283) = 52.3°$.

The regression analyses of stir zone data using the spindle speed (SS)-travel speed (TS)-location in stir zone (LSZ) and θ-α-LSZ bases are shown below.

$$\text{Fraction of Cell Boundaries}_{\text{Predicted}} = 0.771 - 0.049TS + 0.035LSZ$$

$$\text{Fraction of Cell Boundaries}_{\text{Predicted}} = 0.771 + 0.033\theta - 0.036\alpha + 0.035LSZ$$

The SS-TS-LSZ model lies along the negative TS direction in the SS-TS plane as shown in the figure. The θ-α-LSZ is placed arbitrarily on the figure.

If the SS-TS-LSZ model and the θ-α-LSZ model are the same, then $\Phi_1 + \Phi_2 = 90°$.

The angle Φ_2 is defined by $\Phi_2 = \tan^{-1}(0.033/0.036) = 41.8°$, so $\Phi_1 + \Phi_2 = 94.1°$. This verifies that SS-TS-LSZ model and the θ-α-LSZ model are very close to being the same models.

A quick verification of this is to check if $\text{sqrt}(0.033^2 + 0.036^2) = 0.049$, where 0.049 is the coefficient of SS. That calculation checks out, which verifies that the two models are the same.

Figure G- 1 Coordinate axes which compare the spindle speed-travel speed basis model to the alternate tool temperature (θ-α) basis model. The spindle speed-travel speed model is highlighted blue and the θ-α model is highlighted red. The models were first compared vectorially relative to the spindle speed-travel speed basis. The magnitudes of the model coefficients were also compared.

Appendix H. Regression Analyses of TMAZ EBSD Data

The results of regression analyses of TMAZ data are shown in this appendix. The analysis using the spindle speed (SS) and travel speed (TS) is shown in Figure H-1.

```
Predictor       Coef    SE Coef       T       P
Constant    0.795474   0.008511   93.46   0.000
TS         -0.037821   0.009981   -3.79   0.004


S = 0.0282276   R-Sq = 61.5%   R-Sq(adj) = 57.2%


Analysis of Variance

Source           DF         SS         MS      F      P
Regression        1   0.011442   0.011442  14.36  0.004
Residual Error    9   0.007171   0.000797
Total            10   0.018613
```

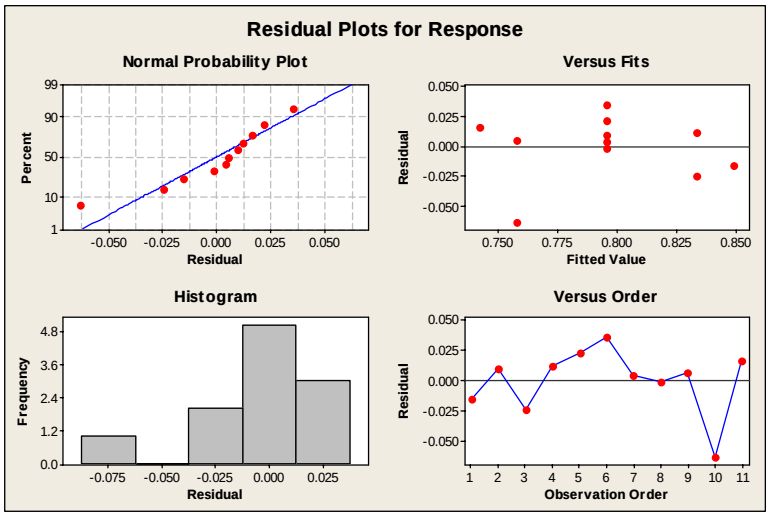

Figure H- 1 ANOVA table and residuals plots for regression analysis of TMAZ data using the spindle speed (SS) and travel speed (TS) basis.

The analysis using the θ and α basis is shown in Figure H-2.

Predictor	Coef	SE Coef	T	P
Constant	0.814994	0.007837	103.99	0.000
θ	0.018461	0.006596	2.80	0.027
α	-0.033535	0.006596	-5.08	0.001
α^2	-0.026842	0.007504	-3.58	0.009

S = 0.0186567 R-Sq = 86.9% R-Sq(adj) = 81.3%

Analysis of Variance

Source	DF	SS	MS	F	P
Regression	3	0.0161765	0.0053922	15.49	0.002
Residual Error	7	0.0024365	0.0003481		
Total	10	0.0186130			

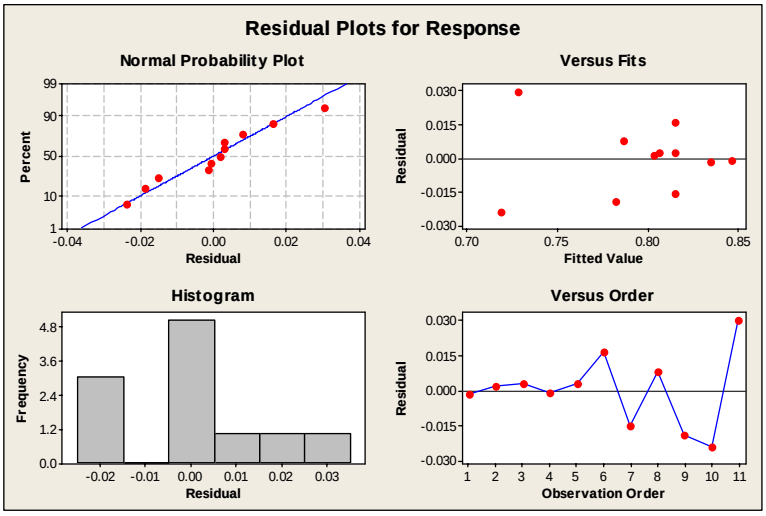

Figure H- 2 ANOVA table and residuals plots for regression analysis of TMAZ data using the θ and α basis.

Appendix I. Comparison of Models of TMAZ Data

The models of the TMAZ data were compared by a process of substitution shown is this appendix. The model obtained using the θ-α basis is shown in Equation I-1.

$$\text{Fraction of Cell Boundaries}_{\text{Predicted}} = 0.815 + 0.018\theta - 0.033\alpha - 0.027\alpha^2 \qquad \text{(I- 1)}$$

The expressions for θ and α that were obtained for the orthonormal basis (see Appendix D) are shown in Equations I-2 and I-3.

$$\theta_{\text{Normalized}} = 0.791\text{SS} - 0.612\text{TS} \qquad \text{(I- 2)}$$

$$\alpha_{\text{Normalized}} = 0.612\text{SS} + 0.791\text{TS} \qquad \text{(I- 3)}$$

Equations I-2 and I-3 are substituted into Equation I-1, which results in Equation I-4. Equation I-4 was used for the model comparisons described in Chapter 4.

$$\begin{aligned}&\text{Fraction of Cell Boundaries}_{\text{Predicted}} \\ &= 0.815 - 0.006\text{SS} - 0.037\text{TS} - 0.026\text{SS x TS} - 0.010\text{SS}^2 - 0.017\text{TS}^2\end{aligned} \qquad \text{(I- 4)}$$